

# Characteristics of Jupiter's X-ray auroral hot spot emissions using Chandra

D. M. Weigt<sup>1</sup>, C. M. Jackman<sup>2</sup>, M. F. Vogt<sup>3</sup>, H. Manners<sup>4</sup>, W. R. Dunn<sup>5</sup>, G. R. Gladstone<sup>6,7</sup>, R. Kraft<sup>8</sup>, G. Branduardi-Raymont<sup>5</sup>, C. K. Louis<sup>2</sup>, S. C. McEntee<sup>2,9</sup>

<sup>1</sup>School of Physics and Astronomy, University of Southampton, Southampton, UK

<sup>2</sup>School of Cosmic Physics, DIAS Dunsink Observatory, Dublin Institute for Advanced Studies, Dublin 15, Ireland

<sup>3</sup>Center for Space Physics, Boston University, Boston, MA, USA

<sup>4</sup>Mullard Space Science Laboratory, Department of Space and Climate Physics, University College London, Dorking, UK

<sup>5</sup>The Centre for Planetary Science at UCL/Birkbeck, London, UK

<sup>6</sup>Space Science and Engineering Division, Southwest Research Institute, San Antonio, TX, USA

<sup>7</sup>Department of Physics and Astronomy, University of Texas at San Antonio, San Antonio, TX, USA

<sup>8</sup>Harvard-Smithsonian Center for Astrophysics, Smithsonian Astrophysical Observatory, Cambridge, MA, USA

USA

<sup>9</sup>School of Physics, Trinity College Dublin, Dublin 12, Ireland

## Key Points:

- We present the first statistical study looking at the behaviour of Jupiter's northern X-ray auroral hot spot from 20 years of Chandra data.
- The X-rays map close to the magnetopause from noon to dusk, with the center of the averaged hot spot emissions mapping to noon.
- Our analysis suggests that the X-ray driver(s) may be linked with ultra-low frequency wave activity along the magnetopause.

---

Corresponding author: Dale Weigt, [D.M.Weigt@soton.ac.uk](mailto:D.M.Weigt@soton.ac.uk)

**Abstract**

To help understand and determine the driver of jovian auroral X-rays, we present the first statistical study to focus on the morphology and dynamics of the jovian northern hot spot (NHS) using Chandra data. The catalogue we explore dates from 18 December 2000 up to and including 8 September 2019. Using a numerical criterion, we characterize the typical and extreme behaviour of the concentrated NHS emissions across the catalogue. The mean power of the NHS is found to be 1.91 GW with a maximum brightness of 2.02 Rayleighs (R), representing by far the brightest parts of the jovian X-ray spectrum. We report a statistically significant region of emissions at the NHS center which is always present, the averaged hot spot nucleus (AHSNuc), with mean power of 0.57 GW and inferred average brightness of  $\sim 1.2$  R. We use a flux equivalence mapping model to link this distinct region of X-ray output to a likely source location and find that the majority of mappable NHS photons emanate from the pre-dusk to pre-midnight sector, coincident with the dusk flank boundary. A smaller cluster maps to the noon magnetopause boundary, dominated by the AHSNuc, suggesting that there may be multiple drivers of X-ray emissions. On application of timing analysis techniques (Rayleigh, Monte Carlo, Jackknife), we identify several instances of statistically significant quasi-periodic oscillations (QPOs) in the NHS photons ranging from  $\sim 2.3$ -min to 36.4-min, suggesting possible links with ultra-low frequency activity on the magnetopause boundary (e.g. dayside reconnection, Kelvin-Helmholtz instabilities).

**Plain Language Summary**

The auroral emissions (northern and southern lights) on Jupiter are the most powerful in our Solar System and have been observed across the electromagnetic spectrum. The cause, or driver, of Jupiter’s auroras is still an open question with lots of scientific debate. The solar wind can have an effect, as can Jupiter’s volcanic moon Io. The plasma and magnetic field interactions can produce auroras on Jupiter in the X-ray waveband. These powerful X-ray emissions can be observed by telescopes like the Chandra X-ray Observatory (CXO) that orbit Earth. The X-ray data we analyze here have been found to flash or pulsate at certain periods, spanning the  $\sim 20$  years Chandra has observed Jupiter. We use mapping and timing analysis techniques to analyze the entire catalogue from the high-resolution camera on-board Chandra. We report significant auroral X-ray regions and pulsations in the north to help us provide an answer for the possible multiple X-ray drivers.

**1 Introduction**

Jupiter has strong auroral X-ray emissions which are observed to be concentrated into a “hot spot”. The first spatially resolved X-ray auroral “hot spot” was observed by Chandra  $\sim 20$  years ago, discovered by Gladstone et al. (2002) in the northern polar region. The term “hot spot” was coined to define the region where most of the X-ray emissions were found from the Chandra observation. Gladstone et al. (2002) defined the hot spot region as a  $5^\circ$  radius circle centered on  $170^\circ$  System III (S3) longitude and  $65^\circ$  latitude. The origin of the ions producing the X-ray emissions were shown to have their source in the outer magnetosphere,  $> 30$  Jupiter radii ( $R_J$ ) from the planet. Timing analysis of the 113 photons within the hot spot showed a flaring of X-ray emissions or quasi-periodic oscillation (QPO) at  $\sim 45$  min, similar to pulsations found in the radio emission from the Ulysses flyby (MacDowall et al., 1993) and electron bursts from the Cassini flyby (Krimigis et al., 2002).

Since then, subsequent Chandra and X-ray Multi-Mirror Mission (XMM-Newton) (Jansen et al., 2001) observations have allowed us to analyze the morphology and composition of the hot spot emissions in more detail at both poles. We now know that the hot spot consists of soft X-rays (SXR, energies  $< 2$  keV) (Branduardi-Raymont et al.,

2008) observed at high latitudes, exhibiting a large range of QPOs (Dunn et al., 2016, 2017; Elsner et al., 2005; Gladstone et al., 2002; Jackman et al., 2018; Kimura et al., 2016; Weigt et al., 2020; Wibisono et al., 2020) which may be correlated with emissions in other wavebands (Dunn et al., 2020a). These SXR are thought to be produced by charge exchange between ions precipitating down into the jovian atmosphere and the neutrals that reside there (Bhardwaj & Gladstone, 2000; Cravens et al., 1995). This heavy ion precipitation can originate from either the open field lines in the magnetosphere connected to the solar wind or on the closed field lines that map to the outer regions of the magnetosphere (Cravens et al., 2003). Energetic heavy ions are found to be the main source of the total X-ray power output (1 GW to a few GWs) (Houston et al., 2020) from the most recent models and *in-situ* Juno data (Bolton et al., 2017). The X-ray auroral spectrum is well-fit by atomic charge exchange spectral lines, with the spectrum typically best fit by an iogenic population of sulfur (S) and oxygen (O) (Elsner et al., 2005; Branduardi-Raymont et al., 2007; Hui et al., 2010; Ozak et al., 2010, 2013; Houston et al., 2020; Dunn et al., 2020b). However, alongside S and O, there are individual observations in which the addition of charge exchange lines from solar wind ions colliding with the atmosphere can improve the spectral fit (Branduardi-Raymont et al., 2007; Hui et al., 2010; Dunn et al., 2020b). In order for this process to operate within the jovian magnetosphere, field-aligned electric fields capable of producing very high potentials ( $\sim 0.2 - 8$  MV) are needed between the ionosphere and magnetosphere (Cravens et al., 2003; Bunce et al., 2004). Such high potentials were observed at Jupiter’s poles by the Jupiter Energetic Particle Detector Instrument (JEDI) (Mauk et al., 2017) on-board Juno. The MV potentials were associated with charge stripping of heavy iogenic ions required for SXR production (Clark et al., 2020). This combination of remote sensing data from the X-ray telescopes and other wavebands with available *in situ* probe data is vital to enhance our understanding of the jovian X-ray emissions. The *in situ* data provides us with the magnetospheric conditions during the observation window, giving the X-ray observations context and determining a possible shared driver across all observed emissions.

The first spatially resolved observation of the southern hot spot was reported by Branduardi-Raymont et al. (2008). Dunn et al. (2017) studied both the northern and southern hot spots for the first time, during an observation when the tilt of the planet was favourable for both poles to be observed. During this observation, the northern and southern hot spots were non-conjugate and found to pulsate at different quasi-periods with a significant 9-11 min QPO in the South and no clear significant pulsations in the North. This suggests that the driver for both hot spots may be different or the same driver was triggered independently in order to produce the different temporal behaviour in the QPOs observed. This independent nature between the hot spots was also found by Weigt et al. (2020). Two significant QPOs were found in the North (lasting for less than one Jupiter rotation) but none in the South, during a  $\sim 10$ -hr Chandra observation (18 June 2017) during Juno apojove (AJ) 6. The magnetosphere was inferred to be compressed during this time from the Jovian Auroral Distributions Experiment (JADE) (McComas et al., 2017) and the Jupiter Energetic Particle Detector (JEDI) (Mauk et al., 2017) on-board Juno. From a concurrent  $\sim 24$ -hr XMM-Newton observation (in which the beginning of the interval overlapped with the final 5 hours of the Chandra campaign), Wibisono et al. (2020) found non-conjugate behaviour simultaneously with Chandra and observed the same significant QPO in the North (26-28 min). However outside of the Chandra window, both the northern and southern auroral regions pulsated with a 23-to 27-min periodicity for  $\sim 12.5$  hours (more than one Jupiter rotation). This suggests that the non-conjugate behaviour of the North and South arises from different drivers producing similar QPOs or as a result from the same driver producing a lag in the emissions we observe (with changing phase). It is apparent from the June 2017 campaigns alone that the emissions from both hot spot emissions are highly variable over a short timescale, raising further questions about the possible drivers capable of producing such pulsed emissions.

129 In order to determine how variable the hot spot temporal and spatial behaviour  
 130 is, we analyze the full Chandra catalogue in a statistical study. This will allow the typ-  
 131 ical and extreme behaviours of the hot spot emissions to be studied in more detail. Find-  
 132 ing these types of behaviour will allow us to have a better grasp of how the X-rays change  
 133 with different magnetospheric conditions (e.g. solar wind, Io activity) which can be ex-  
 134 plored in detail in the future. We apply the algorithm and definitions used by Weigt et  
 135 al. (2020) to find significance in the “average” hot spot morphology (i.e. the occurrence  
 136 of X-ray emissions within the hot spot across all observations) and where the emission  
 137 maps to using a flux equivalence mapping model (Vogt et al., 2011, 2015). To ensure our  
 138 interpretations of the mapping are correct, we explore the limitations and sensitivity of  
 139 the model to possible uncertainties such as the ionospheric position (in jovian S3 lon-  
 140 gitude and latitude coordinates) of the photons detected. From the timing analysis, we  
 141 create a catalogue of results which can be compared to previous statistical studies look-  
 142 ing into the temporal behaviour of the auroral hot spot (such as Jackman et al. (2018))  
 143 and allow us to explore the possible spatial dependence of the QPOs (i.e. are the sig-  
 144 nificant pulsations only found in a particular region of the hot spot?). This allows us to  
 145 check the validity and robustness of our timing analysis as well as comparing any sig-  
 146 nificant QPOs found here to other studies.

147 In section 2, we discuss the Chandra catalogue used in our statistical study and  
 148 the techniques used to process this large data set. Section 3 discusses the average mor-  
 149 phology and the statistical significance of the hot spot emissions. The hot spot emissions  
 150 are then mapped using the Vogt et al. (2011, 2015) method to find the most likely lo-  
 151 cation of the driver, considering possible uncertainties that may have an effect on our  
 152 interpretations. Furthermore, we perform timing analysis on the full Chandra catalogue  
 153 to find and confirm any significant QPOs and explore their possible spatial dependence.  
 154 Section 4 contains a detailed discussion of our results from the statistical study and our  
 155 interpretation of the behaviours observed from the hot spot emissions.

## 156 2 Dataset

157 The data used in this statistical study were obtained by the high-resolution cam-  
 158 era (HRC-I) on board the Chandra X-ray observatory (Weisskopf et al., 2000). The Chan-  
 159 dra HRC-I consists of a single large-format microchannel plate which provides high spa-  
 160 tial resolution of  $\sim 0.4$  arcsec over a  $30$  arcmin  $\times$   $30$  arcmin field of view. The best im-  
 161 age quality is found at the center of the field of view, where the aim point of the cam-  
 162 era is located. Chandra HRC-I can record X-ray photons with energy in the range  $0.08$   
 163 -  $10$  keV. The HRC-I typically observes an average count rate of  $\sim 0.035$  counts/s (with  
 164  $\sim 0.7$  counts/s maximum) from the typically more intense northern auroral X-ray emis-  
 165 sions. The instrument has maximum sensitivity to the lower energy pulsed emissions from  
 166 the SXR’s which allows us to identify clearly the longitude and latitude of the X-ray time-  
 167 tagged photons, with a spatial resolution of  $1^\circ$  S3 longitude  $\times$   $1^\circ$  latitude (after process-  
 168 ing).

169 The Chandra HRC-I data span  $\sim 20$  years with 29 observations in total (to date  
 170 including the Juno era) from 18 December 2000. As shown in Table S1, 8 observations  
 171 spread over several campaigns to coincide with flybys of spacecraft close to Jupiter, or  
 172 to the expected arrival of a coronal mass ejection (CME). This is augmented by 21 ob-  
 173 servations since 2016 spanning the approach phase and early orbits of the Juno space-  
 174 craft. Many of the Chandra campaigns were also carried out in tandem with other re-  
 175 mote sensing observatories (across multiple wavelengths). We only focus on the Chan-  
 176 dra observations in this study which span almost two full solar cycles. All the observa-  
 177 tion dates with the duration, concurrent missions during the Chandra interval and vis-  
 178 ibility of auroral regions are shown in Table S1 in the Supplementary Information, al-  
 179 lowing for future comparative studies. We define the northern auroral region as poleward  
 180 of  $40^\circ$  latitude with an S3 longitude of  $100^\circ$  to  $240^\circ$ . The southern auroral region we de-

181 fine as poleward of  $-60^\circ$  latitude poleward with no longitude constraint as the hot spot  
 182 emissions are more diffuse and are located near the South pole. This therefore makes it  
 183 difficult to find the location of the most intense southern emissions.

184 With the high spatial resolution of Chandra HRC-I, the X-ray emission can be mapped  
 185 onto the jovian disk using 2-D histograms. This is carried out by using the Gaussian point  
 186 spread function (PSF) of the instrument, with a full-width at half maximum (FWHM)  
 187 of 0.4 arcsec, transformed into S3 coordinates. This high spatial resolution allows the  
 188 position and morphology of specific features within the X-ray emissions, such as the hot  
 189 spot, to be spatially down-selected and studied in greater detail. Prior to mapping the  
 190 X-ray emissions, we need to correct for the planet’s motion as it moves across the de-  
 191 tector. Both the data correction and mapping processes are carried out using a Python  
 192 pipeline which assumes the X-ray emissions occur at an altitude of 400 km above the 1-  
 193 bar atmosphere. The PSF size of the HRC is assumed to be 25 arcsec with a FWHM  
 194 of 0.8 arcsec, at variance with the FWHM of the instrument. Further details about the  
 195 Python pipeline can be found in Weigt et al. (2020).

196 With polar projected 2-D histograms mapping X-ray brightness onto Jupiter’s sur-  
 197 face, we can observe the traversal of the hot spot across the disk as Chandra HRC-I ob-  
 198 serves Jupiter. The hot spot traverses the disk for  $\sim 5$  hours, and while most of the ob-  
 199 servations from the Chandra catalogue are  $\sim 10$  hours in duration, some are shorter and  
 200 have been optimized for hot spot viewing. From these observations, 28 out of 29 were  
 201 useable and this is the catalogue we analyze in detail here using our mapping algorithm.  
 202 The observation that could not be mapped properly, ObsID 18303 in Table S1, was un-  
 203 able to be accurately mapped. This resulted from Jupiter being off-center on the detec-  
 204 tor. This misalignment on the detector therefore inhibits optimal mapping of this ob-  
 205 servation as the PSF increases with distance away from the center of the detector. This  
 206 can lead to greater uncertainties when mapping the emissions.

### 207 **3 Results**

208 The specific structures within the X-ray aurora can be studied in more detail by  
 209 defining select spatial regions within the X-ray emissions and analyzing their temporal  
 210 behaviour. Dunn et al. (2020a) recently found that the soft X-ray aurora can be sepa-  
 211 rated into three different sub-categories: regularly pulsed emission, irregularly pulsed emis-  
 212 sion and flickering aurora. The pulsed behaviours were found to be associated with X-  
 213 rays flaring during short-lived ( $\sim 1-2$  min), concentrated intervals which are followed im-  
 214 mediately with longer intervals of dim to no X-ray emissions. The ‘flickering’ behaviour  
 215 of the soft X-ray aurora was observed to vary in brightness over short time scales (1-2  
 216 min) but remained continuous throughout the observation (i.e. no extended intervals de-  
 217 void of X-rays emission). In this study, we will focus on the former two types of X-ray  
 218 aurora where the more intense SXR are found to be concentrated in a hot spot region.  
 219 We analyze in detail the variable spatial and temporal behaviour of these emissions lo-  
 220 cated within this region using a variety of techniques.

#### 221 **3.1 Overall morphological characteristics of the X-ray emissions**

222 With the large catalogue of Chandra HRC-I observations now available, it is now  
 223 possible to explore both the average and extreme conditions of jovian X-ray emissions.  
 224 In this study, we begin by examining planetographic polar projected 2-D histograms of  
 225 the brightness of all auroral X-rays in the catalogue. The polar plots of the averaged X-  
 226 ray emission across the majority of the catalogue (28 observations) are shown in Figure 1.  
 227 The average X-ray emissions were found by mapping all photons in the catalogue to their  
 228 ionospheric positions (S3 longitude, latitude). At each position, the flux found in each  
 229  $1^\circ$  S3 longitude  $\times$   $1^\circ$  latitude bin (the typical spatial resolution of our data) was aver-  
 230 aged over the catalogue, with a typical observation time of  $\sim 10.2$  hours for both the North

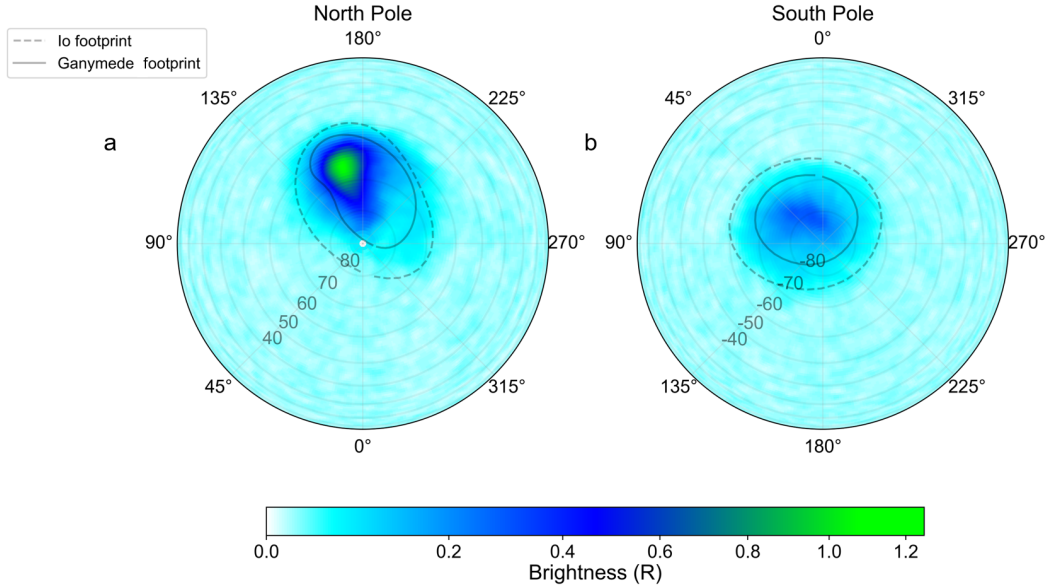


**Figure 1.** Planetographic polar plots of the average X-ray emission as viewed from above (a) Jupiter’s north and (b) south poles from the 28 out of 29 observations of the Chandra HRC-I catalogue. The azimuth angle (in jovigraphic longitude) within the polar plot (in degrees) is indicated around the plot. The concentric circles represent  $10^\circ$  latitude increments with latitudes  $\geq |40^\circ|$  highlighted. The brightness of the X-ray emissions is proportional to the photon flux, calculated from the average point spread function (PSF) across all 29 observations. This is denoted by the color bar below in units of Rayleighs (R). The PSF shows the number density of photons detected with an uncertainty on their position (spreading of the PSF). The regions which have little to no X-ray emissions are represented in white. The Voyager Io Pioneer 4 (VIP4) (Connerney et al., 1998) Io and Grodent Anomaly Model (GAM) (Grodent et al., 2008) Ganymede footprints are plotted in (a) and the VIP4 Io and Ganymede footprints in (b). The footprints in both panels are given by the dashed and solid black lines respectively.

231 and South auroral regions. Such 2-D histograms allow the overall morphology, position  
 232 and properties of the hot spot emissions to be analyzed in greater detail than just the  
 233 photon data alone. Figure 1 shows the X-ray emissions as viewed from above (a) the  
 234 north and (b) south pole. The Grodent Anomaly Model (GAM) (Grodent et al., 2008)  
 235 Ganymede footprint in the North pole is plotted in panel (a). The Voyager Io Pioneer  
 236 4 (VIP4) (Connerney et al., 1998) Io footprint is plotted in both panels and the VIP4  
 237 Ganymede footprint in panel (b). These contours are used in all figures herein for the  
 238 North and South poles and allow us to provide context to the position of the emissions  
 239 on the poles and where they map to magnetically in the magnetosphere.

240 Figure 1 shows a clear asymmetry in the brightness between the North and South  
 241 hot spot (herein referred to as NHS and SHS respectively), as represented by the color  
 242 bar. As depicted in Figure 1a), the most intense NHS emission is located in a tear-drop  
 243 shape with more diffuse emission (dark blue) surrounding the region, extending almost  
 244 out to the pole at S3 longitude of  $0^\circ$ . The more diffuse emissions are located between  
 245 longitudes of  $\sim 90^\circ$  to  $225^\circ$  and are more widespread than the most intense NHS emis-  
 246 sions. The X-rays here are observed to be spread poleward of the Ganymede footprint  
 247 (solid) and extend to the Io footprint (dashed) and beyond in regions closer to  $225^\circ$ .

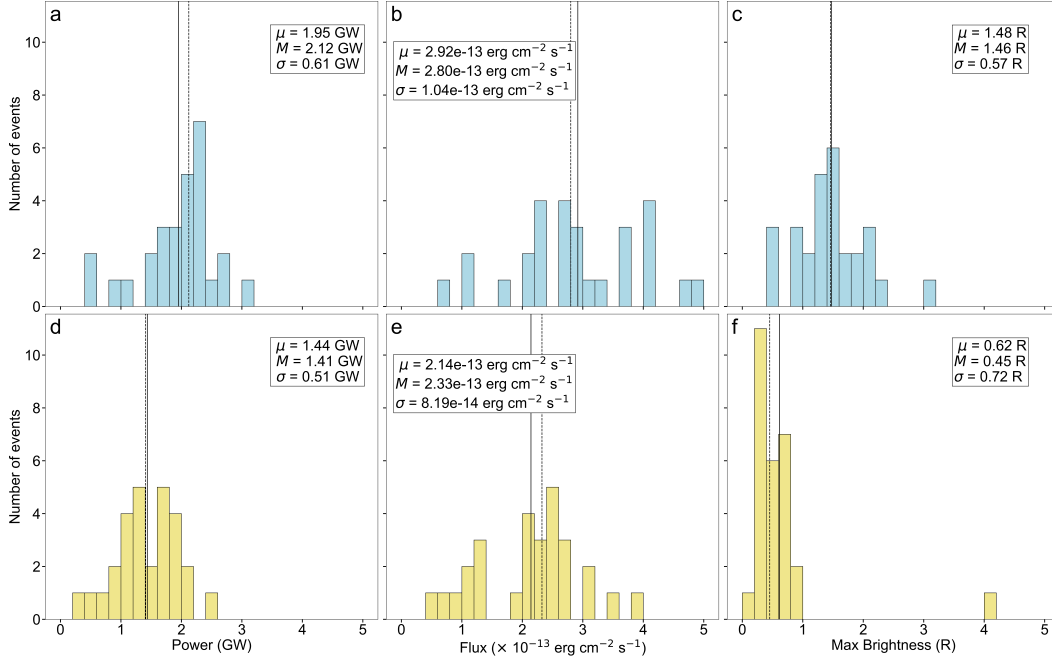


**Figure 2.** Histograms of the properties of the X-ray aurora from the Chandra observation catalogue. Top panels (a) - (c) show values for the North, and bottom panels (d) - (f) show values for the South. First column (panels (a) and (d)) show the power of the X-ray aurora. The following columns show the energy flux ((b) and (e)) and maximum brightness ((c) and (f)) as observed from Chandra (i.e. at Earth). The mean,  $\mu$ , median,  $M$ , and standard deviation,  $\sigma$ , of the distributions are shown in each histogram. The mean and median of each distribution are denoted by the solid and dashed vertical lines respectively.

248 The SHS is observed to be far more diffuse with the most intense emissions located  
 249 within the Ganymede footprint (Figure 1b)). The asymmetry may be a result of unfavourable  
 250 viewing geometry of the SHS throughout the catalogue (Dunn et al., 2017). However,  
 251 in our study, we find this asymmetric auroral behaviour throughout each of the obser-  
 252 vations, including the 12 observations which had equal viewing of both auroral regions  
 253 (Table S1). Therefore viewing geometry may contribute to the non-conjugate behaviour  
 254 but will not be the most dominant effect. The more prominent mechanisms that may  
 255 contribute to the asymmetry may result from the very different magnetic field strengths  
 256 and topologies between both poles (Connerney et al., 2018) as well as possible atmospheric  
 257 effects such as a more opaque atmosphere (Ozak et al., 2010). The polar projected 2-  
 258 D histograms contain no information on the varying opacity of the ionosphere and there-  
 259 fore makes the latter difficult to determine from the Chandra data alone. Therefore, this  
 260 is not the main focus of the study but should be considered in future work.

261 The overall morphology of the brightest SHS emissions is found to be more spot-  
 262 like (i.e. constrained in  $\sim 350^\circ - 60^\circ$  S3 lon and  $\sim 60^\circ$  poleward in latitude) when com-  
 263 pared to its northern counterpart. The spreading of the SHS extends just beyond the  
 264 Ganymede footprint (as shown between an S3 longitude of  $\sim 45^\circ$  and  $180^\circ$ ) similar to  
 265 the NHS. This suggests that the SHS morphology may be very variable across the ob-  
 266 servations or may be another consequence of poorer viewing conditions. The unfavourable  
 267 viewing conditions may impact the accuracy of the SHS mapping.

268 The average powers, energy flux and maximum brightnesses for the North and South  
 269 auroral emissions throughout our catalogue are shown as histograms in Figure 2. The  
 270 values for the mean ( $\mu$ ), median ( $M$ ) and standard deviation ( $\sigma$ ) are displayed in each  
 271 panel with  $\mu$  and  $M$  plotted as the solid and dashed vertical lines respectively. The med-  
 272 ian is calculated for each distribution as the shortest duration observation ( $\sim 3$ -hr ob-  
 273 servation, ObsID 18676) produced an unusual maximum auroral brightness in both pol-  
 274 ar regions (as shown in Figures 2c) and f)). For the power and flux calculation for each  
 275 observation, we assume a photon energy of  $\sim 0.5$  keV (halfway between the sulfur and  
 276 oxygen emission lines), similar to previous work (e.g. Dunn et al. (2016, 2017); Glad-  
 277 stone et al. (2002)). The energy flux we calculate here is the X-ray flux observed from  
 278 Chandra (i.e. at Earth), accounting for the changing Chandra-Jupiter distance over the  
 279 20 year period. We assume that the North and South auroral emission regions account  
 280 for  $\sim 10\%$  and  $\sim 5\%$  of Jupiter’s disk respectively, which is typical of what we observe  
 281 from the Chandra image data. The counts, duration of observation, average angular di-  
 282 ameter of Jupiter and Chandra-Jupiter distance used in our calculations are shown in  
 283 Tables S1 and S2 in the Supplementary Information. We note that the powers and en-  
 284 ergy fluxes calculated for the South are a lower limit due to the poorer viewing geom-  
 285 etry which decreases the number of counts detected by Chandra.

286 As shown in Figures 2a) and d), the mean X-ray auroral power throughout the cat-  
 287 alogue was found to be  $\sim 1.95$  GW and  $1.44$  GW for the North and South respectively  
 288 within the auroral regions defined in Section 2. All our results using the power and flux  
 289 calculations are shown in Table S2. The standard deviations,  $\sigma$ , for all of the distribu-  
 290 tions representing the southern emissions are found to be smaller than their northern  
 291 counterparts. This may suggest that the driver producing the southern auroral X-rays  
 292 and SHS are less variable than those responsible for the northern emissions. The differ-  
 293 ent driver may also contribute to the more diffuse emissions we observe in the South.

294 The auroral powers were found to correspond to an average flux of  $2.92 \times 10^{-13}$   
 295 erg cm $^{-2}$  s $^{-1}$  for the North and  $2.14 \times 10^{-13}$  erg cm $^{-2}$  s $^{-1}$  for the South. The mean  
 296 maximum auroral brightness was observed to be  $1.48$  R (Rayleighs) and  $0.62$  R respec-  
 297 tively, again reflecting the brightness asymmetry between the poles shown in Figure 1.  
 298 The observations throughout the catalogue varied in duration depending on the science  
 299 focus, which may have an effect on the values we calculate here. From the 29 HRC-I ob-  
 300 servations, 6 were optimized for viewing of the intense hot spot region in the north with  
 301 a duration of  $< 1$  jovian rotation. The remaining campaigns lasted for one jovian rota-  
 302 tion or more to explore, in detail, the full X-ray emissions. For the rest of this study, we  
 303 focus in detail on the northern emissions.

### 304 3.2 Exploring the persistence of concentrated NHS auroral photons

305 The average maps in Figure 1 hint at the morphology of the northern auroral X-  
 306 rays, and the structure of the typical northern hot spot embedded in that region, but  
 307 in this section we apply some quantitative criteria to define where photons are concen-  
 308 trated. We build on the method of (Weigt et al., 2020) and define a so-called hot spot  
 309 region across the vast majority of the catalogue. This numerical criterion consists of a  
 310 spatial select region of the hot spot position in the North (S3 longitude:  $100^\circ - 240^\circ$ , lat-  
 311 itude:  $40^\circ - 90^\circ$ , as stated in Section 2) and a numerical threshold on photon concen-  
 312 tration ( $> 7$  photons per  $5^\circ$  S3 lon  $\times$   $5^\circ$  lat) within the NHS. From the Chandra HRC-  
 313 I catalogue, 26 out of the 29 observations had NHS X-ray emissions that were within the  
 314 criterion threshold. Two of the observations (ObsID 15670, 18676) had insufficient counts  
 315 to produce the more highly concentrated NHS emissions. Figure 3 shows plots of a 2-  
 316 D histogram from the resulting emission on a  $3^\circ$  S3 lon  $\times$   $3^\circ$  lat grid and projecting onto  
 317 a planetographic polar map. These plots allow us to determine the typical location of  
 318 the X-rays concentrated within the NHS. The 1-D histograms of S3 longitude and lat-  
 319 itude shown in panel (a) provide a clear representation of the width of the average hot



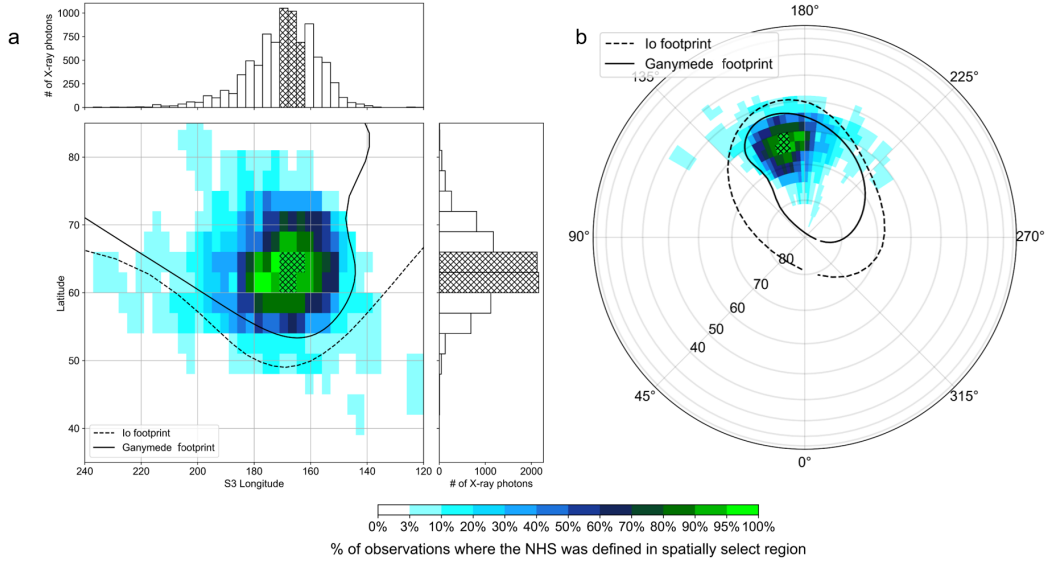


**Figure 3.** (a) Cartesian plot (S3 longitude vs. latitude in degrees) with the number of photons represented as a 1-D histogram of S3 longitude and latitude. The corresponding polar planetographic projection of the NHS X-ray emissions is found using the criterion adapted from Weigt et al. (2020) is shown in (b). The polar plot is of similar format to Figure 1 with binning of  $3^\circ$  S3 lon  $\times$   $3^\circ$  lat. The same binning is used for the histograms, showing more clearly the width of the average hot spot. The Io and Ganymede footprints are plotted in both panels to provide context on the approximate location of the NHS driver. The color bar represents the percentage X-ray photons found across all observations within the spatially select region with the photon concentration threshold applied (26 out of 29 observations from the catalogue). The color bar used in both panels shows what percentage of the observations contained NHS X-ray emissions in each bin. The concentrated X-ray emissions occurring in all observations (100%) in a selected region are denoted by the cross-hatched area in all panels.

spot and highlights the variability within the region. The color bar represents the percentage of observations that had X-rays mapped to a  $3^\circ$  S3 longitude  $\times$   $3^\circ$  latitude bin from 0 - 100%. As highlighted by the cross hatched regions in Figure 3, the NHS always appears in the range  $\sim 162^\circ - 171^\circ$  S3 longitude and  $\sim 60^\circ - 66^\circ$  latitude. This region of interest will be herein referred to as the “averaged hot spot nucleus” or AHSNuc (i.e. with photon concentrations above threshold in 100% of the observations). As the AHSNuc region is found in all observations, this region may map to the location of a physical driving process that is always turned on within the jovian magnetosphere.

From the catalogue of observations, we find that the hot spot often appears (i.e. occurs 70 - 99%) in the range  $\sim 153^\circ - 183^\circ$  S3 longitude and  $\sim 57^\circ - 72^\circ$  latitude, and typically surrounds the AHSNuc. The regions here are found to accompany the central emission throughout the catalogue through possible movement of the hot spot. This would therefore suggest that the driver producing the more intense NHS emissions is often variable, leading to a possible change in morphology and hot spot position. This is further highlighted in the regions where we find that the hot spot is occasionally (i.e occurs between 30% and 70%) found. The emissions here are located at  $\sim 54^\circ - 75^\circ$  latitude and span a slightly larger range of longitudes ( $\sim 150^\circ - 195^\circ$  S3 longitude), falling away from the AHSNuc.

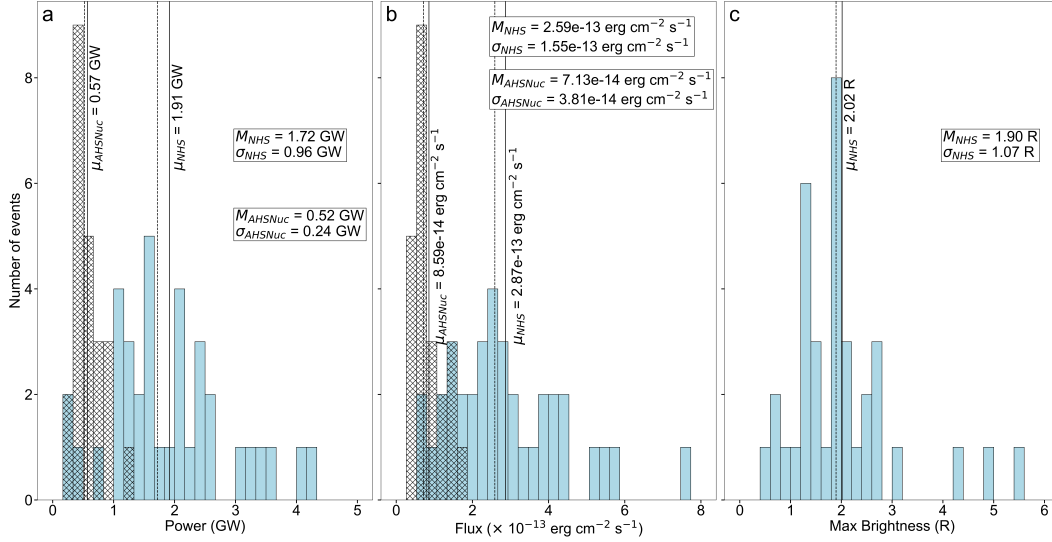


**Figure 4.** Histograms of the same format as Figure 2, showing the average power, flux and maximum brightness of the NHS (blue) and the AHSNuc (cross-hatched). Any overlap of any parameters in the catalogue are shown by the blue, cross-hatched in the histograms. The median and standard deviation values for both regions are shown on the plot. The mean for both the NHS and AHSNuc are shown by the vertical solid lines with the corresponding value displayed alongside. The median for each region is shown by the dashed vertical line. The maximum brightness of the AHSNuc is not shown in panel (c) as finding an accurate brightness over a very small area is difficult to obtain using our current method. The overall average brightness of the AHSNuc can be interpreted from Figure 1

338 The remaining hot spot locations ( $< 30\%$  occurrence) are found to be rare using  
 339 the set criterion and considered extreme hot spot behaviour. From Figure 3 it is clear  
 340 that these regions are more equatorward (beyond the Io footprint in many regions) and  
 341 span the entire longitude range of the Cartesian grid ( $\sim 120^\circ - 237^\circ$  S3 longitude). These  
 342 regions may be a result of other magnetospheric process being activated during the time  
 343 of the observations which may only occur under certain conditions, eluding to a possi-  
 344 bly more fragmented hot spot. The decreasing gradient of the color bar in Figure 3 clearly  
 345 illustrates the variable morphology of the NHS emission across all observations and can  
 346 allow us to analyze further the typical and extreme behaviour of the X-ray auroral emis-  
 347 sions.

348 We apply the same methods described in Section 3.1 to the NHS and AHSNuc to  
 349 produce histograms of the auroral power, flux and maximum brightness in these auro-  
 350 ral features throughout the catalogue (Figure 4). The histograms are of identical format  
 351 to Figure 2. For our calculations, we assume that the emissions observed in the concen-  
 352 trated NHS and AHSNuc cover  $\sim 7\%$  and  $\sim 1\%$  of the jovian disk respectively. This was  
 353 found by comparing the auroral feature in Figure 3 to the overall averaged emissions in  
 354 Figure 1. From Figure 4 we find that the AHSNuc contributes to  $\sim$  one quarter of the  
 355 entire auroral power of the concentrated NHS region ( $0.56$  (AHSNuc) :  $1.91$  (NHS) GW)  
 356 and  $\sim$  one third of the auroral flux ( $0.86$  :  $2.87 \times 10^{-13}$  erg cm $^{-2}$  s $^{-1}$ ). These powers  
 357 and fluxes of the NHS correspond to a mean maximum brightness of  $2.02$  R, represent-  
 358 ing the brightest part of the jovian X-ray spectrum. The standard deviation of the AH-  
 359 SNuc auroral power and flux distribution is less than that found for the NHS, suggest-

ing the driver producing the AHSNuc is less variable. The difference of the distributions for all auroral properties across the NHS and ANHSNuc suggest that multiple drivers producing the X-ray auroral emissions may be plausible. These results suggest that the AHSNuc may be a key auroral feature within the NHS which behaves differently from the full auroral region and must be taken into account in future X-ray auroral studies. However, we do note these results will be further improved with future scheduled Chandra observations and provide more accurate statistics.

The average brightness of the AHSNuc can be inferred from the averaged hot spot emission in Figure 1a). The maximum brightness of the AHSNuc is not shown in Figure 4 as finding an accurate brightness over a very small area is difficult to obtain using our current method. We do note that the three intervals  $2 - 3\sigma$  greater than the mean NHS brightness (ObsID 18678 NHS1, 15671 NHS1 and 18301 NHS1) all correspond the shortest exposure times of the NHS. Similar to the extreme case identified in Figure 2, the shorter exposures times produce more unusual values for the auroral brightness. All results from our calculations of the NHS and AHSNuc for the entire catalogue are shown in Tables S3a and S3b.

The most extreme case of variable morphology was found by Chandra during a  $\sim 20$ -hr ( $\sim 2$  Jupiter rotations) observation on 28 February 2017 (ObsID 20000) during Juno's fourth apojoVe (AJ4). With the longer exposure time, Chandra-HRCI is able collect more photon data. From the criterion, the concentrated emissions were observed over a vast range of longitudes (S3 lon:  $\sim 120^\circ - 237^\circ$ ) and latitudes (lat:  $\sim 39^\circ - 75^\circ$ ). The X-ray aurora within the NHS emitted a power of  $\sim 3.24$  GW (Table S3a). Comparing these numbers with the only other observation that had a duration of  $\sim 2$  Jupiter rotations (ObsID 2519, 25 February 2003), the X-ray aurora within the NHS is found to be  $\sim 7$  times more powerful (0.465 GW) and the region  $\sim 4$  times larger in longitude. As both observations occurred at roughly the same time of year, the seasonal changes between both intervals are very small. Therefore this suggests that the changes in morphology and X-ray power are most likely caused by a change in magnetospheric conditions due to the solar wind or internally from Io.

Another notable observation showcasing the extreme behaviour of the hot spot was found during a  $\sim 7$ -hr observation (ObsID 22159, 8 September 2019) in tandem with Juno perijove (PJ22), optimized for NHS viewing. The emissions here were found to lie within the kink of the GAM Ganymede footprint and extended beyond the Io footprint and were  $\sim 2\sigma$  more powerful (4.03 GW) than the calculated mean power. The only interval that had more powerful auroral emissions was during the second NHS interval during a  $\sim 11$ -hr observation (ObsID 18608, 24 May 2016) at 4.24 GW. The hot spot emission observed from ObsID 22159 was found to reside in a small region (S3 lon:  $\sim 135^\circ - 180^\circ$ ; lat:  $\sim 48^\circ - 66^\circ$ ) with the AHSNuc lying on the edge of the emission. This shows that the driver producing the emissions can also cause variation in the position as well as morphology. The hot spot from ObsID 18608 was found to be located in a similar position to ObsID 22159 with a slightly elongated morphology. The plots of each of the extreme cases mentioned here and all other observations are shown in the Supplementary Information provided (Figure S3). The plots are of the same format as Figure 3 with the color representing the number of photons found in each bin.

### 3.3 Mapping hot spot photons to their magnetospheric origins

In order to map the origin of highly concentrated X-ray emissions of the NHS shown in Figure 3, we use the Vogt et al. (2011, 2015) flux equivalence mapping model. The model relates a region in the ionosphere to source region in the equator. This method assumes that the flux through a given region is located in the jovigraphic equator, which is calculated from the Galileo catalogue with a 2-D fit (radial distance and local time (LT)). The equatorial flux in a given region found from the fit to the data should therefore be

411 equivalent to the flux through the region in the ionosphere to which it maps. The map-  
 412 ping model has a strong dependence on subsolar longitude (SSL) of the photons. The  
 413 mapping model inputs are the ionospheric position (in S3 lon and latitude) and the SSL  
 414 of the time-tagged X-ray photons, which we obtain from the mapping algorithm discussed  
 415 in Weigt et al. (2020). In this study, we use the Vogt et al. model with the internal field  
 416 from GAM. This field model was selected as GAM fits the Ganymede footprint best in  
 417 the north better than VIP4 or VIPAL (Hess et al., 2011) (excepting JRM09 (Connerney  
 418 et al., 2018)). This kink arises from a localized quadrupolar term, introduced in the mag-  
 419 netic field to reproduce the anomaly at the North pole. This will have an effect on the  
 420 more intense regions of the NHS, where the emissions map to in the magnetosphere and  
 421 how we interpret our results.

422 Figure 5a) shows a statistical map of the origins of all mappable photons from Fig-  
 423 ure 3, using the GAM field model and the SSL for each individual photon. A statisti-  
 424 cal map of the location of the possible driver producing the AHSnuc is shown in Figure 5b).  
 425 Their corresponding exposure maps are shown in Figures 5c) and (d), where the num-  
 426 ber of counts are normalized by the length of the observation window. All plots consist  
 427 of a 2-D histogram, showing the number of mapped events ((a) and (b)) and average num-  
 428 ber flux ((c) and (d)), represented by the color bar. The Joy et al. (2002) model limits  
 429 for both a compressed (solar wind dynamic pressure of 0.306 nPa with subsolar distance  
 430  $\sim 60 R_J$ ; black-dashed line) and expanded (0.039 nPa,  $\sim 90 R_J$ ; solid black line) mag-  
 431 netosphere are also plotted to provide context to the mapped origins of the X-ray emis-  
 432 sions. This model combines the observations from multiple spacecraft (Pioneer 10 and  
 433 11, Voyager 1 and 2, Ulysses and Galileo) which crossed Jupiter’s magnetopause bound-  
 434 ary with a magnetohydrodynamics simulation to infer the dynamic pressure of the up-  
 435 stream solar wind and associated subsolar standoff distance. The mapped events have  
 436 been binned by a radial distance of  $10 R_J$  and 1 hour LT. From Figure 5a), it is clear  
 437 that two main populations arise from the analysis: one concentrated on the noon sec-  
 438 tor, and a larger population spread across pre-dusk to pre-midnight of the magnetosphere  
 439 (15 LT - 21 LT), even when corrected for exposure time (Figure 5c)). The majority of  
 440 events in both populations lie close to, in between, or on the magnetopause boundary  
 441 (either expanded or compressed). The population that lies on the pre-dusk to pre-midnight  
 442 magnetopause boundary consists of  $\sim 40\%$  of all mapped photons in the catalogue, sug-  
 443 gesting that this sector of the magnetosphere is the optimum location for the driver of  
 444 ions needed for SXR production. The wedge of high photon counts at 18 LT across all  
 445 radial distances, shown in Figure 5a), disappears in the corresponding exposure map. This  
 446 region was found to be mainly dominated by one observation, ObsID 20000, where the  
 447 most extreme hot spot behaviour was found, as discussed in Section 3.2.

448 The driver producing the AHSnuc is found to lie between noon and 20 LT (Fig-  
 449 ures 5b) and (d)) and consists of  $\sim 7\%$  of all mapped photons in the catalogue. This pop-  
 450 ulation is also found to lie between both magnetopause boundaries, therefore suggest-  
 451 ing that the X-ray driver for the NHS may be sensitive to possible fluctuations in the  
 452 magnetopause location.

453 The Vogt flux equivalence model is built from Galileo data, where the model al-  
 454 gorithm is valid from  $\sim 15 R_J$  (Ganymede footprint) to  $\sim 150 R_J$  (beyond which there  
 455 are insufficient data) and is sensitive to possible changes in ionospheric position. Using  
 456 the flux equivalence model and the same internal field as shown in Figure 5, we estimate  
 457 the errors in mapping that are propagated through from the uncertainty in X-ray pho-  
 458 ton placement. We apply the same  $2.5^\circ$  shifts in latitude and S3 longitude to a grid of  
 459 simulated photons with the same sub-solar longitude (SSL). The resulting plots are shown  
 460 in Figure S1 in the Supplementary Information, illustrating the positions of the origi-  
 461 nal and shifted mapped photons from the grid (in both latitude and longitude separately).  
 462 The shifts used in this study are more extreme than we may observe using the Chan-  
 463 dra HRC-I instrument. The diameter of the Gaussian PSF of the instrument is smaller

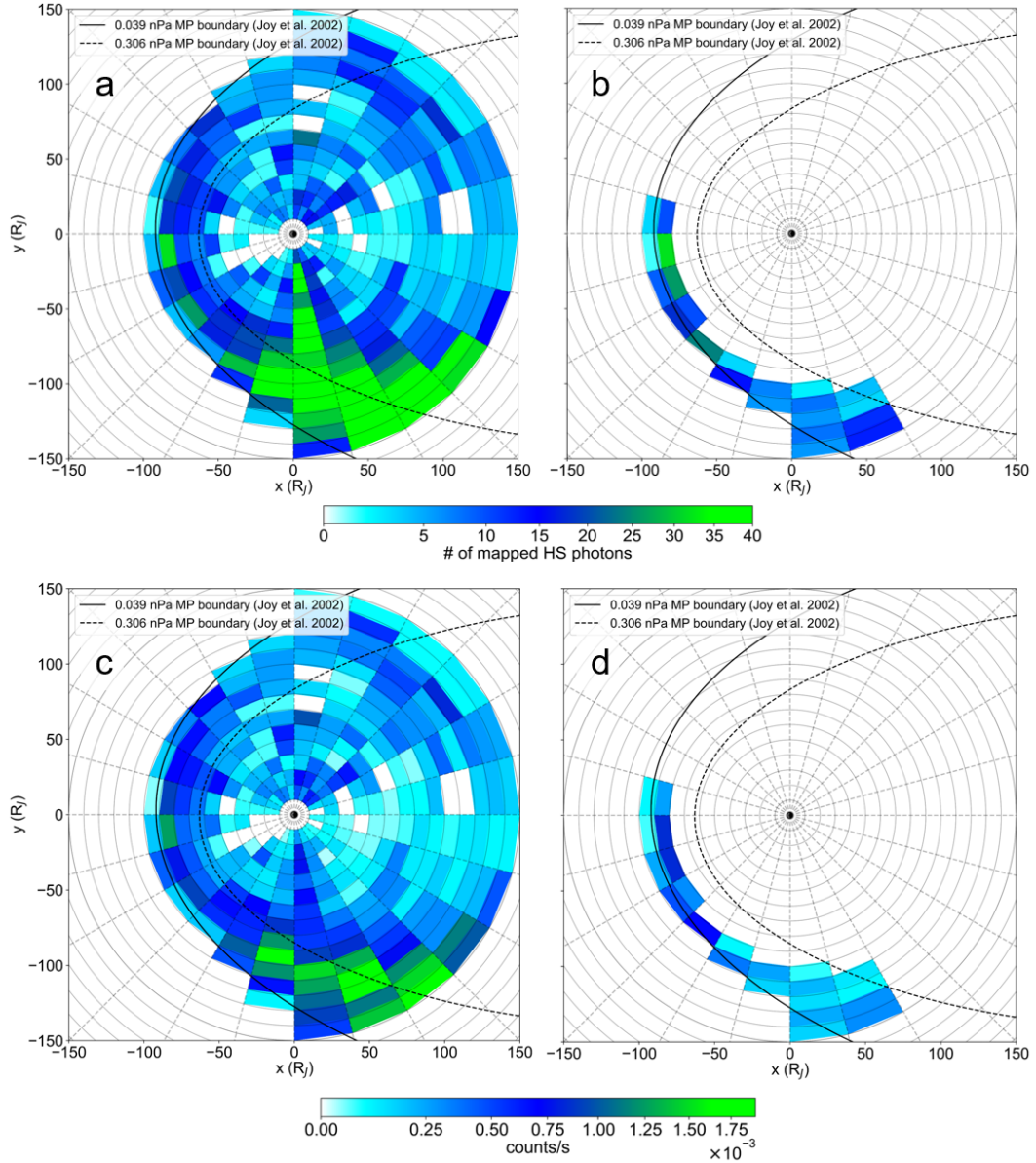


**Figure 5.** Plot of (a) all the mapped photons and (b) the mapped origin of the AHSNuc photons within the threshold for 26 out of 29 observations. The corresponding exposure maps are shown in (c) and (d), where each photon mapped has been normalized by the length of window observed for each event in the catalogue. The photons are mapped using the Vogt flux equivalence mapping model using GAM. The concentric circles in (a) - (d) represent the distance from Jupiter in  $10 R_J$  increments. The Joy et al. (2002) compressed (black dashed line) and expanded (solid black line) magnetopause boundary limits are also plotted. The mapped data are binned by a radial distance of  $10 R_J$  and a local time (LT) of 1 hour. The color bar represents the number of events found (panels (a) and (b)) and the average number flux (counts/s) in each bin (panels (c) and (d)).

464 than the  $2.5^\circ$  shift used here as we can resolve the center of the PSF (photon ionospheric  
 465 positions) to  $1^\circ$  S3 lon  $\times$   $1^\circ$  lat. From comparing both panels, a shift in either latitude  
 466 and S3 longitude results in different changes in both radial distance and local time de-  
 467 pending on where the origin is within the jovian magnetosphere. This means that mapped  
 468 photons that lie on or close to a magnetopause boundary may be interpreted as beyond  
 469 or within the magnetopause region; a caveat we take into account when interpreting our  
 470 results. The magnetopause is also not a static location and so mapping to it is not ex-  
 471 act (using any model). The mapping uncertainty from ionospheric position will there-  
 472 fore be affected by magnetospheric conditions as well as the strong dependence on SSL.  
 473 Therefore calculating the full error on mapping is very difficult and not the main focus  
 474 of this study.

475 As the flux equivalence model uses Galileo data, where the magnetosphere was mainly  
 476 expanded or returning to an equilibrium state throughout the campaign, observations  
 477 during a compression are more difficult to model. As a result, we interpret events in be-  
 478 tween both Joy model limits and close to the compressed boundary to lie in a region on  
 479 the magnetopause boundary or just outside the magnetosphere. It is therefore clear that,  
 480 on average, most of the intense NHS emission is found to originate on/near the magne-  
 481 topause boundary pre-dusk to pre-midnight. Vogt et al. (2019) highlight that a compres-  
 482 sion event can contribute to a shift in ionospheric position of the main auroral emissions  
 483 towards the jovian magnetic pole. Such shifts can change the magnetospheric mapping  
 484 of the static (non time dependent) flux equivalence model of up to tens of  $R_J$ . This ef-  
 485 fect, in addition to the strong SSL dependence, may be responsible for the spread of the  
 486 main mapped drivers in Figure 5 on the noon and dusk boundary. Finally, we show com-  
 487 parisons with an applied shift in ionospheric position and compare to JRM09 in the Sup-  
 488 plementary Information provided (Figure S2). This shows how the interpretation of the  
 489 driver may be affected depending on the field model used in concert with the Vogt et al.  
 490 flux equivalence model.

### 491 3.4 Searching for quasi-periodic NHS emissions

492 Following the Rayleigh test techniques outlined in Jackman et al. (2018) and Weigt  
 493 et al. (2020), we search for quasi-periodicity or quasi-periodic oscillations (QPOs) in the  
 494 catalogue. Figure 6 show the results of the timing analysis for the QPOs found within  
 495 the (a) NHS region and (b) AHSNuc. The QPOs identified with a significance below our  
 496 99% significance threshold or  $p$ -value ( $p > 0.01$ ) are represented by the gray distribu-  
 497 tion. The  $p$ -value here is defined to be the probability of obtaining results at least as ex-  
 498 treme as the observed data assuming a correct null hypothesis, in this case no periodic  
 499 signal. Any QPOs found from the timing analysis with statistical significance  $\geq 99\%$  ( $p$   
 500  $\leq 0.01$ ) are shown in solid blue and green for the NHS and AHSNuc regions respectively.  
 501 The striped distributions represent QPOs found with significance  $\geq 99.999\%$  ( $p \leq 10^{-5}$ ).  
 502 The results for all observations used in the Figures 3 - 6 for the NHS and AHSNuc are  
 503 show in Tables S4 and S5 in the Supplementary Information.

504 The Rayleigh test was carried out for each interval the concentrated X-ray emis-  
 505 sions were detected by the instrument during the observation (Tables S4 and S5). This  
 506 therefore allows us to determine each time the NHS is in view by setting a limit of the  
 507 time interval between the time-tagged photons. We set a time limit of  $> 180$  min be-  
 508 tween time-tagged photons to define each time the NHS is in Chandra's field of view.  
 509 The duration of each viewing of the NHS, average Chandra-Jupiter distance over the in-  
 510 terval, total counts and count rate are given to allow us to ensure there were enough pho-  
 511 tons detected to produce a power spectrum that represented the Chandra data well. Any  
 512 observations with counts  $< 30$  were removed from the analysis. The next columns show  
 513 the proportion of photons mapped in these regions, shown in Figure 5. From both ta-  
 514 bles,  $\sim 90\%$  of observations have  $< 50\%$  of photons mapped using the Vogt et al. (2011,  
 515 2015) flux equivalence model. This may be due to the fact that much of the NHS and

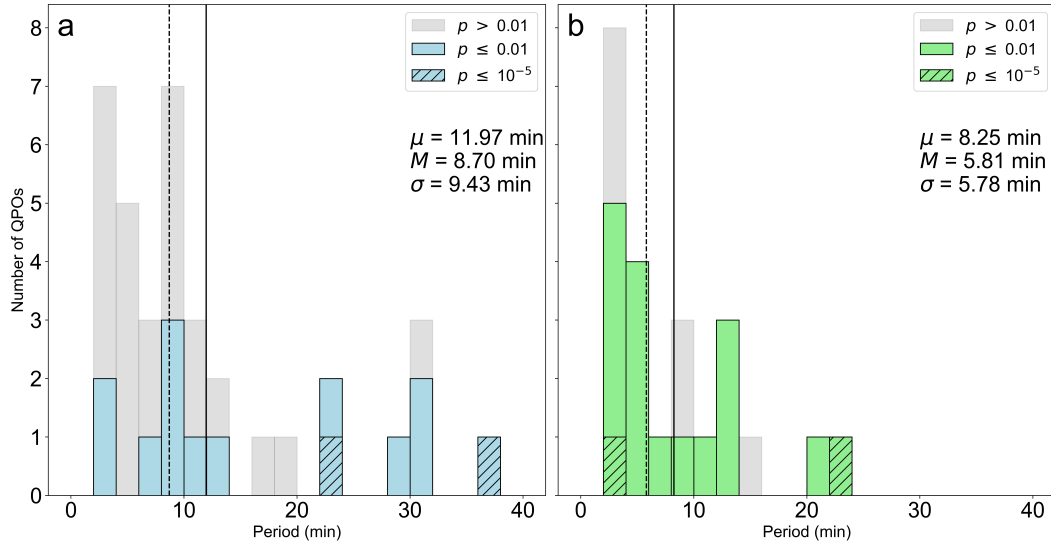


**Figure 6.** Histogram of the Rayleigh test results from the (a) full NHS and (b) AHSNuc throughout the catalogue (as shown in Tables S4 and S5). The histogram is of identical format to Figures 2 and 4. The gray distribution on both panels represents the QPOs found throughout the catalogue with a statistical significance  $< 99\%$  or  $p$ -value ( $p$ )  $> 0.01$ . The solid blue and green bars show the number of QPOs with significance  $\geq 99\%$  ( $p \leq 0.01$ ) and the striped bars represent a  $p \leq 10^{-5}$  (significance  $\geq 99.999\%$ ).

516 AHSNuc either maps outside the model constraints ( $< 15R_J$  or  $> 150 R_J$ ) and/or the  
517 mapping is limited by the SSL during the observation, resulting in poorer viewing con-  
518 ditions for most observations.

519 The timescales of the significant QPOs throughout the catalogue are found to be  
520  $\sim 3.9 - 36.4$  min and  $\sim 2.3 - 22.4$  min for the NHS region and AHSNuc respectively. The  
521 difference in QPO ranges are a result of down-selecting from the larger, full NHS region  
522 to the smaller AHSNuc, a specific feature in the auroral emissions. The change of pe-  
523 riods show that in many cases the full hot spot auroral region does not pulsate simul-  
524 taneously and that smaller structures within the hot spot can pulsate independently from  
525 the surrounding auroral emissions. As shown in Tables S4 and S5, the longest QPO, with  
526  $p \leq 10^{-5}$ , was found during the first interval the NHS was observed on 18 June 2017 (Ob-  
527 sID 20001) and is in agreement with the results found by Weigt et al. (2020). The only  
528 QPOs found from the AHSNuc  $> 2\sigma$  of the mean period were from ObsID 22146 (*sim*  
529 7-hr observation optimized for hot spot viewing on 13 July 2019) and ObsID 20733 NHS2  
530 (second NHS interval of  $\sim 11$ -hr observation on 1 April 2018) at 21.7 and 22.4 mins re-  
531 spectively. We find in many observations, the NHS and AHSNuc are found to both pro-  
532 duce significant QPOs during the same interval (e.g. ObsID 15669, 18677, 22146). Dur-  
533 ing three intervals (ObsID 16299 NHS2, 20002, 20733 NHS2) the NHS and AHSNuc were  
534 found to produce the same significant QPO, suggesting that the dominant driver(s) pro-  
535 ducing the auroral emissions were associated with the AHSNuc.

536 Many of the QPOs found here agree with the values found by the timing analy-  
537 sis study of Jackman et al. (2018). In their study they noted that differences in QPO  
538 period (and associated significance) are highly sensitive to the selection of the hot spot.  
539 Their work explored the entire northern (and southern) auroral region, with a simple down-  
540 select for hot spot based on viewing a time window as the hot spot traversed the disk.  
541 Here we employ a more strict spatial criterion for hot spot selection, and, while for most

542 examples, our results are broadly in line with those of Jackman et al. (2018), there are  
 543 examples where the period and the significance differ. This shows how sensitive the QPOs  
 544 are to the selection of the hot spot - and thus in turn, perhaps, how tightly constrained  
 545 the driver of the periodic emission is. We also note that there is no clear correlation be-  
 546 tween the average Chandra-Jupiter distance and detection of significant QPOs in both  
 547 the full auroral region and the AHSNuc (Tables S4 and S5) as well as any distance de-  
 548 pendent auroral parameters (i.e. flux, power). We would expect the closer Jupiter is to  
 549 the instrument, the easier it would be to detect significant QPOs with brighter and more  
 550 powerful aurora which we do not observe here. Therefore, we can rule out distance as  
 551 a parameter than can influence detecting the X-ray emissions and inhibit our timing anal-  
 552 ysis to detect statistically significant QPOs.

553 We further improve the significance of the signals found here by testing the sensi-  
 554 tivity of each of the light curves to the observed frequency of the signal. We do this  
 555 by using a Jackknife test (Quenouille, 1949, 1956), by removing a number of photons from  
 556 each of the light curves and running the Rayleigh test algorithm, using an identical fre-  
 557 quency space, on each new light curve (Efron & Stein, 1981). All the power spectra gener-  
 558 ated are then plotted together and the time interval between the minimum and maxi-  
 559 mum period found,  $\Delta P$ , is measured. This allows us to provide an estimate of the sensi-  
 560 tivity of each light curve to frequency. As Chandra has a poor throughput and there-  
 561 fore observes very few photons, the Jackknife test used in this study removed a maxi-  
 562 mum of two photons each time, ensuring that there was no degeneracy from the selec-  
 563 tion process. Tables 1 and 2 show the results of the Jackknife test for the removal of one  
 564 photon (JK1) and two photons (JK2) for each of the QPO datasets shown in Figure 6  
 565 above our 99% significance threshold. The first column in both tables gives the unique  
 566 Chandra ObsID for each observation. The following columns gives the region and inter-  
 567 val during the observation window (i.e. NHS2 = NHS observed for the 2nd time, and  
 568 similarly for AHSNuc) and the results from JK1 and JK2. The nomenclature and for-  
 569 mating are similar to Tables S3 and S4 in the Supplementary Information. All the hot  
 570 spot observations with a  $\Delta P > 5$  min are bold text. These QPOs, although statistically  
 571 significant from the Rayleigh test, are found to be not robust and highly sensitive to fre-  
 572 quency. As a result, we remove these periods from the catalogue, reducing the signifi-  
 573 cant QPOs from 14 to 12 for the NHS region and 17 to 9 for the AHSNuc. The light curves  
 574 found for the AHSNuc contained far fewer photons and are therefore more sensitive to  
 575 the Jackknife test. However, we do note that this test does not account for the coher-  
 576 ence (i.e. how sinusoidal) of the QPO signal. The more coherent signals will produce a  
 577 smaller  $\Delta P$  value from both Jackknife tests. Therefore some of the QPOs removed from  
 578 the catalogue may still be robust but with a non-sinusoid envelope. Future temporal stud-  
 579 ies may want to consider the coherence in their timing analysis to avoid the possible bias  
 580 from such tests, although this is non-trivial to implement when used with the Rayleigh  
 581 test.

582 The range of quasi-periods found from our catalogue may correspond to a variety  
 583 of possible drivers. The vast range in significant QPOs found suggest that the X-ray driver  
 584 may be connected with ultra-low frequency (ULF) waves along the magnetopause bound-  
 585 ary. Pulsations  $\sim 5$ -60 min from standing Alfvén waves have been found throughout the  
 586 jovian magnetosphere (Manners et al., 2018). The QPOs produced by the AHSNuc may  
 587 be associated with possible pulsed dayside reconnection on the magnetopause. Bunce  
 588 et al. (2004) found that such reconnection could produce pulsations of  $\sim 30$ -50-min and  
 589 is more active during magnetospheric compressions. This therefore may be responsible  
 590 for the larger QPOs found in our catalogue. Combining both our timing and mapping  
 591 results, we suggest that there are multiple drivers producing the X-rays along the mag-  
 592 netopause boundary from noon to the dusk flank. Figures 5 and 6 show the possibil-  
 593 ity of strong contributions from multiple drivers which may either be semi-permanent  
 594 or more sporadic in nature.



**Table 1.** Table of Chandra ObsID, hot spot interval and results of the Jackknife test performed on statistically significant QPOs found in the NHS

ObsID	Region	JK1 <sup>a</sup> ( $\Delta P$ (mins))	JK2 <sup>b</sup> ( $\Delta P$ (mins))
15669	NHS2	0.000	0.000
<b>15671</b>	<b>NHS2</b>	<b>19.742</b>	<b>19.921</b>
15672	NHS2	0.063	0.063
<b>16299</b>	<b>NHS2</b>	<b>0.000</b>	<b>9.803</b>
16300	NHS	0.000	0.223
18608	NHS1	0.000	0.000
18609	NHS	0.000	0.000
18677	NHS	0.237	0.473
20000	NHS3	0.000	0.000
20001 <sup>†</sup>	NHS1	0.570	0.852
20002	NHS	0.000	0.000
20733 <sup>†</sup>	NHS2	0.000	0.175
22146	NHS	0.000	0.000
22148	NHS	0.000	0.000

*Note.* <sup>a</sup>Results from Jackknife test removing 1 photon.

<sup>b</sup> Results from Jackknife test removing 2 photons.

<sup>†</sup> Hot spot intervals with a 99.999% sig. QPO.

**Table 2.** Table of Chandra ObsID, hot spot interval and results of the Jackknife test performed on statistically significant QPOs found in the AHSNuc

ObsID	Region	JK1 <sup>a</sup> ( $\Delta P$ (mins))	JK2 <sup>b</sup> ( $\Delta P$ (mins))
<b>15669</b>	<b>AHSNuc</b>	<b>7.236</b>	<b>7.236</b>
<b>15671</b>	<b>AHSNuc2</b>	<b>19.388</b>	<b>19.564</b>
<b>15672</b>	<b>AHSNuc2</b>	<b>0.291</b>	<b>9.777</b>
<b>16299</b>	<b>AHSNuc</b>	<b>0.106</b>	<b>9.826</b>
18302	AHSNuc	0.000	3.198
18608	AHSNuc2	0.000	0.041
18677	AHSNuc	0.049	0.049
<b>18678</b>	<b>AHSNuc</b>	<b>11.398</b>	<b>11.398</b>
20001	AHSNuc1	0.072	4.182
20002 <sup>†</sup>	AHSNuc	0.000	0.622
<b>20733</b>	<b>AHSNuc1</b>	<b>0.065</b>	<b>64.1806</b>
20733 <sup>†</sup>	AHSNuc2	0.351	0.702
22146	AHSNuc	0.171	0.512
22147	AHSNuc	0.034	0.034
22148	AHSNuc	4.048	4.048
<b>22151</b>	<b>AHSNuc</b>	<b>0.000</b>	<b>5.681</b>
<b>22159</b>	<b>AHSNuc2</b>	<b>8.013</b>	<b>8.013</b>

*Note.* Identical format to Table 1

## 4 Discussion

The results of our statistical study analyzing the Chandra HRC-I dataset allows us, for the first time, to explore in detail the statistical significance of the variability in morphology of the X-ray emissions and their origin. We adapt the Weigt et al. (2020) numerical criterion to define the highly concentrated NHS emissions, allowing us to hone on the QPO regions and their associated magnetospheric drivers.

### 4.1 Characteristics and polar conjugacy of auroral X-ray emissions

The polar plots and histograms we present in Section 3.1 clearly show an asymmetry in brightness and morphology across the catalogue between the North and more diffuse South. This asymmetry has been observed in previous case studies (e.g. Dunn et al. (2017); Weigt et al. (2020)) and is believed to possibly result from a combination of unfavourable viewing geometry of the south due to Jupiter’s tilt (Dunn et al., 2017); the radically different magnetic field strength and topology at the poles found by Juno magnetometer data (Connerney et al., 2017, 2018) and the opacity of the jovian atmosphere (Ozak et al., 2010). The North polar region is observed to have a non-dipolar field topology and is more than twice as strong as the more dipole-like South pole (Moore et al., 2018). The difference in magnetic field magnitude may effect the mechanism(s) that allow the ions to be injected into the ionosphere at the poles. The most plausible explanation for this arises from the stronger non-dipolar north producing a stronger mirror force than its southern dipolar counterpart. This will produce the large potential drop required to accelerate the ions (both solar wind and iogenic in origin) to the larger energies needed for ion precipitation in the ionosphere to produce the X-ray aurora (Cravens et al., 2003; Houston et al., 2020). This process may favour the slightly extended tear-drop morphology we observe here in the brightest North emissions. Since the configuration of the North polar region is more non-dipolar and producing a stronger magnetic field strength, the mirror force would be greater. This would lead to more ions being trapped, leading to more ions being accelerated to the energies required for precipitation than in the South. A similar mechanism may operate in the South where the mirror force will be weaker and therefore fewer ions will be accelerated to the required energies for precipitation, leading to dimmer X-ray emissions.

Recent work by Dunn et al. (2020a) classified the X-ray aurora into three categories from Chandra and XMM-Newton observations in 2007: hard X-ray (energies  $> 2$  keV) bremsstrahlung main emission; pulsed SXR emissions (both regular and irregular) and dim flickering (quasi-continuously present emission, varying on very short timescales). They identified that the X-ray emissions were dominated by pulsed SXR emissions, mainly produced from iogenic ions. They found that the brightest X-ray aurora coincided with magnetospheric expansions and was found to have a more patchy and extended morphology. The aurora during a compression was found to be more concentrated into a localized bright region at S3 longitudes of  $\sim 160^\circ$  to  $180^\circ$ . The polar plots of the extended North emission reflect this behaviour across the catalogue, showing the variation of the magnetospheric conditions throughout the catalogue. The extended emission is found to be more spread and diffuse with a localized bright tear-drop around  $180^\circ$  S3 lon in the center (see Figure 1). The brightest emission residing within this tear-drop region lies in roughly the same location as the *core region* of the X-ray emission, observed by Kimura et al. (2016) during an UV and X-ray campaign in 2014. Therefore this region may be a recurring characteristic of the X-ray auroral emissions.

Many previous case studies have analyzed the X-ray emissions during times of compression (Dunn et al., 2016; Wibisono et al., 2020; Weigt et al., 2020). They found localized brightenings within the northern auroral emissions (Dunn et al., 2016) and an extended morphology (Weigt et al., 2020) during a compression event. Wibisono et al. (2020) found that iogenic ions are responsible for the emissions with very little contri-

646 bution from the solar wind during magnetospheric compression. Kimura et al. (2016)  
 647 however found that the count rate of the core region during the 2014 campaign was posi-  
 648 tively correlated with the solar wind velocity as opposed to morphology. The flux within  
 649 this region however may change due to the changing dynamic pressure caused by the so-  
 650 lar wind's effect on the magnetosphere as opposed to a direct effect on the X-ray emis-  
 651 sion itself. Therefore, the variable morphologies we see in the northern X-ray aurora (as  
 652 classified by (Dunn et al., 2020a)) may be a result of changing dynamic pressure and re-  
 653 flect the jovian magnetosphere's sensitivity to such changes.

#### 654 **4.2 Morphological variability and origins of the concentrated NHS emis-** 655 **sions**

656 The polar projected 2-D histograms of hot spot location and histograms of the au-  
 657 roral properties in Section 3.2 depict the typical and extreme behaviour of the concen-  
 658 trated NHS X-ray emissions. For the first time, we find a statistically significant region  
 659 in the NHS emission, AHSNuc, using the numerical threshold previously defined. The  
 660 less variable AHSNuc (Figure 4) provides further evidence supporting the X-ray emis-  
 661 sions are highly concentrated, which can be mapped to specific driver mechanisms. Ex-  
 662 ternal mechanisms, like the solar wind ram pressure, may affect the morphology of the  
 663 emission surrounding the AHSNuc in the same way as the averaged X-ray auroral emis-  
 664 sions.

665 The typical behaviour of the NHS (occurrences of  $> 70\%$  in the catalogue shown  
 666 in Figure 3) is found to be confined within an ellipse of semi-major axis  $\sim 15^\circ$  and semi-  
 667 minor axis  $\sim 7.5^\circ$ , centered at ( $168^\circ$  S3 lon,  $65^\circ$  lat). Within this region, the gradient  
 668 of the photon occurrence is found to vary at higher longitudes away from the AHSNuc.  
 669 This may be evidence of further segregation that has been alluded to occur during a com-  
 670 pression event (Dunn et al., 2016; Weigt et al., 2020) and may be the locations for con-  
 671 centrated X-ray emission to brighten during these times, as found by Dunn et al. (2020a).  
 672 The more extreme behaviour (occurrences  $\leq 20\%$ ) we observe from the NHS emissions  
 673 surrounds the ellipse defining more typical behaviour. This region of extreme behaviour  
 674 may be a result of a lower solar wind dynamic pressure causing an expansion of the mag-  
 675 netosphere. Therefore our study suggests very few X-ray observations in the catalogue  
 676 coincided with an expansion event.

677 Figure 5 shows the resultant mapping using the Vogt et al. (2011, 2015) flux equiv-  
 678 alence model with the Grodent Anomaly Model (GAM) (Grodent et al., 2008) option.  
 679 The model finds two ion populations along the magnetopause boundary when mapping  
 680 the NHS: a significantly large population in the pre-dusk to pre-midnight sector, coin-  
 681 cident with the dusk flank and a smaller cluster at noon. The former population iden-  
 682 tified in this study agrees with previous work using the Vogt model to determine the ori-  
 683 gin of the NHS (Kimura et al., 2016; Dunn et al., 2017; Weigt et al., 2020). The driver  
 684 producing such emissions was suggested to be related with Kelvin-Helmholtz instabil-  
 685 ities (KHIs) on the dusk flank. KHIs along the magnetopause boundary are responsi-  
 686 ble for energy, momentum and plasma transfer between the magnetosheath and the mag-  
 687 netosphere. Such phenomena have previously been observed at Jupiter's magnetopause  
 688 boundary (Delamere & Bagenal, 2010; Desroche et al., 2012) where the velocity shear  
 689 between solar wind flow and sheath flow is greatest. These instabilities are predicted to  
 690 be predominantly found on the dusk side of the boundary at Jupiter (Zhang et al., 2018).  
 691 This contradicts the expectation where shear flows are expected to be maximized in the  
 692 pre-noon sector where plasma from the magnetosheath and magnetosphere flow in op-  
 693 posite directions. This has also been observed At Saturn (e.g. (Masters et al., 2012; De-  
 694 lamere et al., 2013)) where it is theorised that the dawn-dusk asymmetry may arise from  
 695 fast-growing KHIs at dawn being difficult to identify from the spacecraft data in com-  
 696 parison to the more easily detected slow-growing KHIs at dusk (Ma et al., 2015). This

697 is consistent with what we observe here as the Vogt et al. flux equivalence model uses  
698 Galileo data to trace the origins of the ions in the magnetosphere.

699 The equatorial conjugate positions in the magnetosphere of both populations identified  
700 in this study are also consistent with the location of ultra-low frequency (ULF) activity  
701 found by Manners and Masters (2020). The most active regions were found to be  
702 near noon at a distance of  $\sim 40 - 100 R_J$  and the dusk-midnight sector, primarily confined  
703 along the magnetopause at a distance of  $\sim 20 - 120 R_J$ . The power of the ULF waves  
704 produced was found to decrease with increasing distance out into the outer magnetosphere,  
705 where the X-ray ions are believed to be located ( $> 60 R_J$  (Dunn et al., 2016)). KHIs on  
706 the magnetopause boundary have been observed to trigger ULF wave activity in Earth's  
707 magnetosphere (Hasegawa et al., 2004) and possibly trigger reconnection within the vortices  
708 (Nykyri & Otto, 2001). With the coincident location of the ULF waves and X-ray  
709 producing ions, the drivers of the X-ray emissions may be linked to possible ULF wave  
710 activity in the jovian magnetosphere.

### 711 4.3 Timescales of possible noon and dusk flank X-ray drivers

712 Throughout the literature about the jovian magnetosphere, there have been many  
713 theories hypothesizing the driver of the emissions we believe to originate on the mag-  
714 netopause boundary. In the noon sector, Bunce et al. (2004) proposed a cusp recon-  
715 nection model as a strong candidate for the X-ray driver, producing  $\sim 30$ - to  $50$ -min QPOs.  
716 The fast flow model predicts that X-ray emissions produced by cusp reconnection will  
717 have a brightness, on average, of  $\sim$  few Rayleighs (R), which we do observe in the AH-  
718 SNuc (see Figure 1), up to a few kR (kilo-Rayleighs). We also observe comparable auroral  
719 power to the predicted power from the Bunce et al. model. The cusp model may  
720 therefore provide a case for the driver we observe on the noon magnetopause boundary.  
721 The intensity of the X-ray emissions may be greater than our results suggests due to the  
722 poor throughput of the instrument and/or the opacity of the atmosphere (Ozak et al.,  
723 2010). Therefore, the AHSNuc may be driven by cusp reconnection and the variable QPOs  
724 dependent on reconnection activity, linked to solar wind flow.

725 Guo et al. (2018) found signatures of rotationally driven magnetic reconnection from  
726 magnetometer and charged particle data in Saturn's dayside magnetodisk. They reported  
727 multiple reconnection sites and a secondary magnetic island, eluding to a non-steady state  
728 process. Such a mechanism may operate in Jupiter's rapidly rotating magnetosphere and  
729 produce similar pulsations to those predicted by the cusp model. Magnetic reconnection  
730 has been observed on the dawn flank of the jovian magnetopause by Juno (Ebert et al.,  
731 2017), where it is believed to play a more significant role in jovian magnetospheric dy-  
732 namics during times of compression (Huddleston et al., 1997). This suggests that both  
733 cusp and rotationally driven reconnection may be plausible. Therefore, both recon-  
734 nection phenomena may be the driver for the noon ion population dominated by the AH-  
735 SNuc, where the majority of mapped events are found.

736 Previous studies analyzing the X-ray aurora suggest that the quasi-periodic emis-  
737 sions may be a result of global ULF waves in the magnetic field. ULF waves have been  
738 observed ubiquitously throughout the jovian magnetosphere (e.g. (Khurana & Kivelson,  
739 1989; Wilson & Dougherty, 2000)) lying within the  $10$ - to  $60$ -min QPO range proposed  
740 by Manners et al. (2018) for standing Alfvén waves, and just one possible driver of many  
741 suggested possibilities. This ULF period range is similar to what was found in a recent  
742 study using a more complicated model to simulate field resonances within the jovian mag-  
743 netosphere to improve our understanding of Jupiter's magnetospheric response to such  
744 magnetic fluctuations (Lysak & Song, 2020).

745 This type of wave may be a by-product of KHIs on the magnetopause boundary.  
746 Both the dayside reconnection processes described by Bunce et al. (2004) and Guo et  
747 al. (2018) may be linked to linear sinusoidal KHI waves known as surface waves. These

748 surface waves have been observed to drive standing Alfvén waves in the terrestrial iono-  
 749 sphere (Mann et al., 2002; Rae et al., 2005) and could propagate ULF wave activity from  
 750 the outer jovian magnetosphere to the ionosphere as found by Manners and Masters (2020).  
 751 Both simulations and observation data suggest that the linear KHI waves on the day-  
 752 side boundary ( $> 10$  LT) may be advected to the dusk flank, in the direction of increas-  
 753 ing velocity shear (Zhang et al., 2018; Manners & Masters, 2020). With the increase in  
 754 velocity shear, the KHI waves transition from a steady sinusoidal linear wave to a non-  
 755 linear KHI wave, with rolled vortices and a greater amplitude. These waves tend to be  
 756 found in KH-unstable regions on the dawn and dusk sectors of the magnetopause, first  
 757 suggested by Dungey (1955), where the instability can grow. For the terrestrial case, the  
 758 thickness and location of such unstable regions are dependent of the angle of the inter-  
 759 planetary magnetic field (IMF) (Farrugia et al., 1998; Foullon et al., 2008). The IMF an-  
 760 gle also produces a dawn-dusk asymmetry when the northward field is tilted westwards  
 761 which may explain the asymmetries we expect at Jupiter (Zhang et al., 2018). At the  
 762 time of writing, very little has been observed regarding possible KH-unstable regions at  
 763 Jupiter. Masters (2018) suggested that viscous-like effects, such as KHIs within KH-unstable  
 764 regions, are likely to dominate over reconnection-type effects at Jupiter compared to Earth.  
 765 This is in agreement with the possible correlation between X-rays and ULF wave activ-  
 766 ity we find in this study. With the extension of the Juno science mission, Juno will be  
 767 located within the dawn-midnight magnetosphere where activity within the dusk flanks  
 768 can be explored in more detail.

769 From their extensive study of heritage jovian magnetometer data, Manners and Mas-  
 770 ters (2020) found ULF QPOs, associated with standing Alfvén waves, spanning  $\sim 5$ -60  
 771 min across all local times from the Galileo mission (Russell, 1992) and fly-bys performed  
 772 by Voyager 1 and 2 (Kohlhase & Penzo, 1977), Pioneer 10 and 11 (Northrop et al., 1974;  
 773 Sandel et al., 1975) and Ulysses (Wenzel et al., 1992). Galileo observed the jovian mag-  
 774 netosphere across a large span of local times with most of its coverage in the dusk-dawn  
 775 sector. The QPOs found from the heritage magnetometer data are consistent with the  
 776 significant quasi-periods we report here. In the kronian magnetosphere, previous stud-  
 777 ies have found pulsations of  $\sim 35$  - 50 min from possible KHI waves on the dawn and  
 778 dusk flank of the magnetopause from Cassini magnetometer data (Cutler et al., 2011;  
 779 Masters et al., 2009). As this lies within the ULF periodicity range, the idea behind low-  
 780 amplitude ULF wave energy accumulating in the dusk flank from advected waves from  
 781 the noon sector may be plausible. The mechanism by which ULF wave energy modu-  
 782 lates the local ion populations so that they are so energized and pitch-angle scattered  
 783 into the loss cone is still speculative. The KHIs along the dusk flank may also be reflected  
 784 by the different X-ray auroral morphologies identified by Dunn et al. (2020a). During  
 785 compression events, the magnetopause standoff distance is closer to the planet and there-  
 786 fore the dusk flank shrinks. As the boundary is smaller, fewer but more powerful KHI  
 787 waves may be produced driving the ULF wave activity to produce localized X-ray bright-  
 788 ening. The more patchy morphology observed during an expanded magnetosphere may  
 789 be a result of more vortices generating less powerful KHI waves. This suggests that the  
 790 “hot spot” may be a result of multiple processes and not confined to a single spot re-  
 791 gion, as previously theorized. Therefore using such nomenclature, like “hot spot”, maybe  
 792 unsuitable to describe these phenomena.

793 Our mapping and timing analysis shown here allow for the possibility that mul-  
 794 tiple drivers, including, but not limited to, cusp/dayside reconnection and KHIs along  
 795 the noon-dusk magnetopause boundary may be driving the X-ray emission. These drivers  
 796 may be connected to ULF wave activity which is present throughout the jovian magne-  
 797 tosphere and pulsations similar to those found in our catalogue. The drivers on the noon  
 798 and dusk magnetopause boundary may be linked to possible ULF wave activity high-  
 799 lighted by Manners and Masters (2020). How they are linked (i.e possible ULF waves  
 800 from dayside reconnection, advected to the nightside? greater velocity shears on the dusk  
 801 flank?) is still not fully understood but we have provided the foundations to allow fur-

802 ther study into this relatively unknown region. Future studies should consider combin-  
 803 ing models of the X-ray emissions within the northern auroral region and new *in situ* ob-  
 804 servations with Juno’s evolving trajectory, moving past midnight toward the dusk flank.  
 805 This will allow us to delve further into exploring the ULF wave activity on the dusk flank  
 806 and if it is connected to the pulsating X-ray emissions we observe.

## 807 5 Summary

808 From the ever expanding catalogue of Chandra HRC-I observations of jovian X-  
 809 rays across multiple solar cycles and various solar wind and magnetospheric conditions,  
 810 we present the first statistical study of its kind to analyze typical and extreme “hot spot”  
 811 behaviour. We perform mapping and timing analysis techniques to try and determine  
 812 any statistical significance within the location and pulsations of the hot spot and where  
 813 they map to in the jovian system. This statistical study included all Chandra HRC-I data  
 814 to date. We identify a statistically significant region of concentrated X-ray auroral emis-  
 815 sions within the hot spot that appear in all observations in the catalogue, the AHSNuc,  
 816 using the numerical criterion adapted from Weigt et al. (2020). This region maps mainly  
 817 to the noon magnetopause boundary. All the concentrated X-ray photons that lie within  
 818 the Weigt et al. (2020) numerical threshold are found to populate the noon magnetopause  
 819 boundary (dominated by the AHSNuc) and the dusk flank boundary. The results pre-  
 820 sented here suggest that the X-rays originate from multiple drivers that may be linked  
 821 to possible ULF wave activity on the magnetopause boundary. The mechanisms we sug-  
 822 gest capable of accelerating the ions to the required precipitation energies are dayside  
 823 reconnection and KHIs along the magnetopause boundary. These processes may be linked  
 824 through possible advection of ULF waves from noon to dusk, producing stronger non-  
 825 linear KHI waves along KH-unstable regions. We frame these observations with previ-  
 826 ous key studies analyzing the X-ray aurora; models suggesting plausible drivers and ULF  
 827 wave activity in the jovian magnetosphere, providing the foundations for future stud-  
 828 ies.

829 We hope that the work presented here helps narrow down the list of possible drivers  
 830 that produce the X-ray auroral emissions using a consistent definition and numerical thresh-  
 831 old and sets the foundations for further exploration. The idea of the soft X-rays being  
 832 confined to a single “hot spot” (i.e. produced by one driver) seems less likely from the  
 833 results we show here. It is clear that in order to fully understand the driver and vari-  
 834 ability of the X-ray aurora, we need to apply these techniques to multiwavelength data  
 835 (both *in situ* and remote sensing data such as XMM-Newton and the Hubble Space Tele-  
 836 scope (HST)) to find any key correlations. With Juno’s extended science mission tak-  
 837 ing the spacecraft through dusk-midnight sector, a similar statistical study can be car-  
 838 ried out for the South pole with comparisons made between the poles. From there, we  
 839 can then truly understand how the X-rays behave on a more planet-wide scale and the  
 840 implications that has on the possible drivers as well as allowing us to fully understand  
 841 the asymmetries we observe between North and South in X-rays and across many wave-  
 842 lengths.

## 843 Acknowledgments

844 D. M. W. is supported by the Science and Technology Facilities Council (STFC) stu-  
 845 dentship ST/S505705/1. C. M. J.’s work at DIAS is supported by the Science Founda-  
 846 tion Ireland (SFI) Grant 18/FRL/6199. C. K. L and S. C. M are also supported by SFI  
 847 grant 18/FRL/6199. H. M. is supported by a Royal Society PhD studentship. W.R.D.  
 848 was supported by a STFC research grant ST/S000240/1 to University College London  
 849 (UCL). G. B.–R. acknowledges partial support from STFC Consolidated Grant ST/S000240/1  
 850 to UCL. This research has made use of data obtained from the *Chandra Data Archive*  
 851 and *Chandra Source Catalogue* (<https://cda.harvard.edu/chaser/>). The data required

852 to reproduce the results shown in this study are stored in the Zenodo repository at DOI:  
853 10.5281/zenodo.4275744.

## 854 References

- 855 Bhardwaj, A., & Gladstone, G. R. (2000). Auroral emissions of the giant planets.  
856 *Reviews of Geophysics*, *38*(3), 295–353. doi: 10.1029/1998RG000046
- 857 Bolton, S. J., Lunine, J., Stevenson, D., Connerney, J. E. P., Levin, S., Owen,  
858 T. C., ... Thorpe, R. (2017). The Juno Mission. *Space Science Reviews*,  
859 *213*(1-4), 5–37. Retrieved from <http://dx.doi.org/10.1007/s11214-017-0429-6>  
860 <http://link.springer.com/10.1007/s11214-017-0429-6> doi:  
861 10.1007/s11214-017-0429-6
- 862 Branduardi-Raymont, G., Bhardwaj, A., Elsner, R. F., Gladstone, G. R., Ramsay,  
863 G., Rodriguez, P., ... Cravens, T. E. (2007). Latest results on Jovian disk  
864 X-rays from XMM-Newton. *Planetary and Space Science*, *55*(9), 1126–1134.  
865 doi: 10.1016/j.pss.2006.11.017
- 866 Branduardi-Raymont, G., Elsner, R. F., Galand, M., Grodent, D., Cravens, T. E.,  
867 Ford, P., ... Waite, J. H. (2008). Spectral morphology of the X-ray emis-  
868 sion from Jupiter’s aurorae. *Journal of Geophysical Research: Space Physics*,  
869 *113*(2), 1–11. doi: 10.1029/2007JA012600
- 870 Bunce, E. J., Cowley, S. W., & Yeoman, T. K. (2004). Jovian cusp processes: Impli-  
871 cations for the polar aurora. *Journal of Geophysical Research: Space Physics*,  
872 *109*(A9), 1–26. doi: 10.1029/2003JA010280
- 873 Clark, G., Mauk, B. H., Kollmann, P., Paranicas, C., Bagenal, F., Allen, R. C., ...  
874 Westlake, J. H. (2020). Heavy Ion Charge States in Jupiter’s Polar Magneto-  
875 sphere Inferred From Auroral Megavolt Electric Potentials. *Journal of Geo-*  
876 *physical Research: Space Physics*, *125*(9), 1–12. doi: 10.1029/2020ja028052
- 877 Connerney, J. E., Acuña, M. H., Ness, N. F., & Satoh, T. (1998). New models  
878 of Jupiter’s magnetic field constrained by the Io flux tube footprint. *Jour-*  
879 *nal of Geophysical Research: Space Physics*, *103*(A6), 11929–11939. doi:  
880 10.1029/97ja03726
- 881 Connerney, J. E., Benn, M., Bjarno, J. B., Denver, T., Espley, J., Jorgensen, J. L.,  
882 ... Smith, E. J. (2017). The Juno Magnetic Field Investigation. *Space Science*  
883 *Reviews*, *213*(1-4), 39–138. Retrieved from <http://dx.doi.org/10.1007/s11214-017-0334-z> doi: 10.1007/s11214-017-0334-z
- 884 Connerney, J. E., Kotsiaros, S., Oliverson, R. J., Espley, J. R., Joergensen, J. L.,  
885 Joergensen, P. S., ... Levin, S. M. (2018). A New Model of Jupiter’s Magnetic  
886 Field From Juno’s First Nine Orbits. *Geophysical Research Letters*, *45*(6),  
887 2590–2596. doi: 10.1002/2018GL077312
- 888 Cravens, T. E., Howell, E., Waite, J. H., & Gladstone, G. R. (1995). Auroral oxygen  
889 precipitation at Jupiter. *Journal of Geophysical Research*, *100*(A9), 17153. doi:  
890 10.1029/95ja00970
- 891 Cravens, T. E., Waite, J. H., Gombosi, T. I., Lugaz, N., Gladstone, G. R., Mauk,  
892 B. H., & MacDowall, R. J. (2003). Implications of Jovian X-ray emission for  
893 magnetosphere-ionosphere coupling. *Journal of Geophysical Research: Space*  
894 *Physics*, *108*(A12), 1–12. doi: 10.1029/2003JA010050
- 895 Cutler, J. C., Dougherty, M. K., Lucek, E., & Masters, A. (2011). Evidence of sur-  
896 face wave on the dusk flank of Saturn’s magnetopause possibly caused by the  
897 Kelvin-Helmholtz instability. *Journal of Geophysical Research: Space Physics*,  
898 *116*(10), 1–9. doi: 10.1029/2011JA016643
- 899 Delamere, P. A., & Bagenal, F. (2010). Solar wind interaction with Jupiter’s magne-  
900 tosphere. *Journal of Geophysical Research: Space Physics*, *115*(10), 1–20. doi:  
901 10.1029/2010JA015347
- 902 Delamere, P. A., Wilson, R. J., Eriksson, S., & Bagenal, F. (2013). Magnetic  
903 signatures of Kelvin-Helmholtz vortices on Saturn’s magnetopause: Global  
904



- 905 survey. *Journal of Geophysical Research: Space Physics*, 118(1), 393–404. doi:  
906 10.1029/2012JA018197
- 907 Desroche, M., Bagenal, F., Delamere, P. A., & Erkaev, N. (2012). Conditions at  
908 the expanded Jovian magnetopause and implications for the solar wind inter-  
909 action. *Journal of Geophysical Research: Space Physics*, 117(7), 1–18. doi:  
910 10.1029/2012JA017621
- 911 Dungey, J. W. (1955). Electrodynamics of the Outer Atmosphere. In *Physics*  
912 *of the ionosphere, report of the conference held at the cavendish labo-*  
913 *ratory* (p. 229). Physics Society of London, London. Retrieved from  
914 <https://ui.adsabs.harvard.edu/abs/1955phio.conf..229D>
- 915 Dunn, W. R., Branduardi-Raymont, G., Carter-Cortez, V., Campbell, A., Elsner,  
916 R., Ness, J.-U., ... Achilleos, N. (2020b). Jupiter’s X-ray Emission During the  
917 2007 Solar Minimum. *Journal of Geophysical Research: Space Physics*, 125(6),  
918 e2019JA027219. Retrieved from [https://onlinelibrary.wiley.com/doi/](https://onlinelibrary.wiley.com/doi/abs/10.1029/2019JA027219)  
919 [abs/10.1029/2019JA027219](https://onlinelibrary.wiley.com/doi/abs/10.1029/2019JA027219) doi: 10.1029/2019JA027219
- 920 Dunn, W. R., Branduardi-Raymont, G., Elsner, R. F., Vogt, M. F., Lamy, L., Ford,  
921 P. G., ... Jasinski, J. M. (2016). The impact of an ICME on the Jovian X-ray  
922 aurora. *Journal of Geophysical Research A: Space Physics*, 121(3), 2274–2307.  
923 doi: 10.1002/2015JA021888
- 924 Dunn, W. R., Branduardi-Raymont, G., Ray, L. C., Jackman, C. M., Kraft, R. P.,  
925 Elsner, R. F., ... Coates, A. J. (2017). The independent pulsations of Jupiter’s  
926 northern and southern X-ray auroras. *Nature Astronomy*, 1(11), 758–764.  
927 Retrieved from <http://dx.doi.org/10.1038/s41550-017-0262-6> doi:  
928 10.1038/s41550-017-0262-6
- 929 Dunn, W. R., Gray, R., Wibisono, A. D., Lamy, L., Louis, C., Badman, S. V., ...  
930 Kraft, R. (2020a). Comparisons Between Jupiter’s X-ray, UV and Radio  
931 Emissions and InSitu Solar Wind Measurements During 2007. *Journal of Geo-*  
932 *physical Research: Space Physics*, 125(6), e2019JA027222. Retrieved from  
933 <https://onlinelibrary.wiley.com/doi/abs/10.1029/2019JA027222> doi:  
934 10.1029/2019JA027222
- 935 Ebert, R. W., Allegrini, F., Bagenal, F., Bolton, S. J., Connerney, J. E., Clark, G.,  
936 ... Wilson, R. J. (2017). Accelerated flows at Jupiter’s magnetopause: Evi-  
937 dence for magnetic reconnection along the dawn flank. *Geophysical Research*  
938 *Letters*, 44(10). doi: 10.1002/2016GL072187
- 939 Efron, B., & Stein, C. (1981). The Jackknife Estimate of Variance. *The Annals*  
940 *of Statistics*, 9(3), 586–596. Retrieved from [http://projecteuclid.org/](http://projecteuclid.org/euclid.aos/1176345976)  
941 [euclid.aos/1176345976](http://projecteuclid.org/euclid.aos/1176345976)[http://projecteuclid.org/euclid.aos/](http://projecteuclid.org/euclid.aos/1176348654)  
942 [1176348654](http://projecteuclid.org/euclid.aos/1176348654)<http://projecteuclid.org/euclid.aos/1176345462> doi:  
943 10.1214/aos/1176345462
- 944 Elsner, R. F., Lugaz, N., Waite, J. H., Cravens, T. E., Gladstone, G. R., Ford, P.,  
945 ... Majeed, T. (2005). Simultaneous Chandra X ray Hubble Space Telescope  
946 ultraviolet, and Ulysses radio observations of Jupiter’s aurora. *Journal of Geo-*  
947 *physical Research: Space Physics*, 110(A1), 1–16. doi: 10.1029/2004JA010717
- 948 Farrugia, C. J., Gratton, F. T., Bender, L., Biernat, H. K., Erkaev, N. V., Quinn,  
949 J. M., ... Dennisenko, V. (1998). Charts of joint Kelvin-Helmholtz and  
950 Rayleigh-Taylor instabilities at the dayside magnetopause for strongly north-  
951 ward interplanetary magnetic field. *Journal of Geophysical Research: Space*  
952 *Physics*, 103(A4), 6703–6727. doi: 10.1029/97ja03248
- 953 Foullon, C., Farrugia, C. J., Fazakerley, A. N., Owen, C. J., Gratton, F. T., & Tor-  
954 bert, R. B. (2008). Evolution of Kelvin-Helmholtz activity on the dusk flank  
955 magnetopause. *Journal of Geophysical Research: Space Physics*, 113(11), 1–22.  
956 doi: 10.1029/2008JA013175
- 957 Gladstone, G. R., Waite, J. H., Grodent, D., Lewis, W. S., Crary, F. J., Elsner,  
958 R. F., ... Cravens, T. E. (2002). A pulsating auroral X-ray hot spot  
959 on Jupiter. *Nature*, 415(6875), 1000–1003. Retrieved from <http://>

- 960 [www.nature.com/articles/4151000a](http://www.nature.com/articles/4151000a) doi: 10.1038/4151000a
- 961 Grodent, D., Bonfond, B., Gérard, J. C., Radioti, A., Gustin, J., Clarke, J. T., ...  
 962 Connerney, J. E. (2008). Auroral evidence of a localized magnetic anomaly  
 963 in Jupiter's northern hemisphere. *Journal of Geophysical Research: Space*  
 964 *Physics*, 113(9), 1–10. doi: 10.1029/2008JA013185
- 965 Guo, R. L., Yao, Z. H., Sergis, N., Wei, Y., Mitchell, D., Roussos, E., ... Wan,  
 966 W. X. (2018). Reconnection Acceleration in Saturn's Dayside Magnetodisk:  
 967 A Multicase Study with Cassini. *The Astrophysical Journal*, 868(2), L23.  
 968 Retrieved from <http://dx.doi.org/10.3847/2041-8213/aaedab> doi:  
 969 10.3847/2041-8213/aaedab
- 970 Hasegawa, H., Fujimoto, M., Phan, T.-D., Rème, H., Balogh, A., Dunlop, M. W., ...  
 971 Tandokoro, R. (2004). Transport of solar wind into Earth's magnetosphere  
 972 through rolled-up Kelvin-Helmholtz vortices. *Nature*, 430(7001), 755–758. doi:  
 973 10.1038/nature02799
- 974 Hess, S. L., Bonfond, B., Zarka, P., & Grodent, D. (2011). Model of the Jovian mag-  
 975 netic field topology constrained by the Io auroral emissions. *Journal of Geo-*  
 976 *physical Research: Space Physics*, 116(5), 1–19. doi: 10.1029/2010JA016262
- 977 Houston, S. J., Cravens, T. E., Schultz, D. R., Gharibnejad, H., Dunn, W. R.,  
 978 Haggerty, D. K., ... Ozak, N. (2020). Jovian Auroral Ion Precipitation:  
 979 XRay Production From Oxygen and Sulfur Precipitation. *Journal of Geo-*  
 980 *physical Research: Space Physics*, 125(2), 2019JA027007. Retrieved from  
 981 <https://onlinelibrary.wiley.com/doi/10.1029/2019JA027007> doi:  
 982 10.1029/2019JA027007
- 983 Huddleston, D. E., Russell, C. T., Le, G., & Szabo, A. (1997). Magnetopause struc-  
 984 ture and the role of reconnection at the outer planets. *Journal of Geophysical*  
 985 *Research A: Space Physics*, 102(A11), 24289–24302. doi: 10.1029/97JA02416
- 986 Hui, Y., Schultz, D. R., Kharchenko, V. A., Bhardwaj, A., Branduardi-Raymont, G.,  
 987 Stancil, P. C., ... Dalgarno, A. (2010). Comparative analysis and variability  
 988 of the Jovian X-ray spectra detected by the Chandra and XMM-Newton obser-  
 989 vatories. *Journal of Geophysical Research: Space Physics*, 115(A7), 1–19. doi:  
 990 10.1029/2009ja014854
- 991 Jackman, C. M., Knigge, C., Altamirano, D., Gladstone, R., Dunn, W., Elsner, R.,  
 992 ... Ford, P. (2018). Assessing Quasi-Periodicities in Jovian X-Ray Emissions:  
 993 Techniques and Heritage Survey. *Journal of Geophysical Research: Space*  
 994 *Physics*, 123(11), 9204–9221. doi: 10.1029/2018JA025490
- 995 Jansen, F., Lumb, D., Altieri, B., Clavel, J., Ehle, M., Erd, C., ... Vacanti, G.  
 996 (2001). XMM-Newton spacecraft and operations. *Astronomy and Astrophysics*,  
 997 365, L1–L6. doi: 10.1051/0004-6361
- 998 Joy, S. P., Kivelson, M. G., Walker, R. J., Khurana, K. K., Russell, C. T., & Ogino,  
 999 T. (2002). Probabilistic models of the Jovian magnetopause and bow shock  
 1000 locations. *Journal of Geophysical Research: Space Physics*, 107(A10), 1–17.  
 1001 doi: 10.1029/2001JA009146
- 1002 Khurana, K. K., & Kivelson, M. G. (1989). Ultralow frequency MHD waves in  
 1003 Jupiter's middle magnetosphere. *Journal of Geophysical Research*, 94(A5),  
 1004 5241. doi: 10.1029/ja094ia05p05241
- 1005 Kimura, T., Kraft, R. P., Elsner, R. F., Branduardi-Raymont, G., Gladstone, G. R.,  
 1006 Tao, C., ... Murray, S. S. (2016). Jupiter's X-ray and EUV auroras moni-  
 1007 tored by Chandra, XMM-Newton, and Hisaki satellite. *Journal of Geophysical*  
 1008 *Research A: Space Physics*, 121(3), 2308–2320. doi: 10.1002/2015JA021893
- 1009 Kohlhase, C., & Penzo, P. (1977). Voyager mission description. *Space Science*  
 1010 *Reviews*, 21(2). Retrieved from [http://link.springer.com/10.1007/](http://link.springer.com/10.1007/BF00200846)  
 1011 [BF00200846](http://link.springer.com/10.1007/BF00200846) doi: 10.1007/BF00200846
- 1012 Krimigis, S. M., Mitchell, D. G., Hamilton, D. C., Dandouras, J., Armstrong, T. P.,  
 1013 Bolton, S. J., ... Williams, D. J. (2002). A nebula of gases from Io surround-  
 1014 ing Jupiter. *Nature*, 415(6875), 994–996. doi: 10.1038/415994a

- 1015 Lysak, R. L., & Song, Y. (2020). Field Line Resonances in Jupiter’s Magnetosphere.  
 1016 *Geophysical Research Letters*, *47*(18). doi: 10.1029/2020GL089473
- 1017 Ma, X., Stauffer, B., Delamere, P. A., & Otto, A. (2015). Asymmetric Kelvin-  
 1018 Helmholtz propagation at Saturn’s dayside magnetopause. *Journal of Geophys-*  
 1019 *ical Research: Space Physics*, *120*(3), 1867–1875. Retrieved from [http://doi](http://doi.wiley.com/10.1002/2014JA020746)  
 1020 [.wiley.com/10.1002/2014JA020746](http://doi.wiley.com/10.1002/2014JA020746) doi: 10.1002/2014JA020746
- 1021 MacDowall, R. J., Kaiser, M. L., Desch, M. D., Farrell, W. M., Hess, R. A., & Stone,  
 1022 R. G. (1993). Quasiperiodic Jovian Radio bursts: observations from the  
 1023 Ulysses 1. MacDowall, R. J. et al. Quasiperiodic Jovian Radio bursts: observa-  
 1024 tions from the Ulysses Radio and Plasma Wave Experiment. *Planet. Space Sci.*  
 1025 *41*, 10591072 (1993). Radio and Plasma Wave Ex. *Planetary and Space Science*,  
 1026 *41*(11-12), 1059–1072. doi: 10.1016/0032-0633(93)90109-F
- 1027 Mann, I. R., Voronkov, I., Dunlop, M., Donovan, E., Yeoman, T. K., Milling, D. K.,  
 1028 ... Opgenoorth, H. J. (2002). Coordinated ground-based and Cluster ob-  
 1029 servations of large amplitude global magnetospheric oscillations during a  
 1030 fast solar wind speed interval. *Annales Geophysicae*, *20*(4), 405–426. doi:  
 1031 10.5194/angeo-20-405-2002
- 1032 Manners, H., & Masters, A. (2020). The Global Distribution of UltraLowFre-  
 1033 quency Waves in Jupiter’s Magnetosphere. *Journal of Geophysical Research:*  
 1034 *Space Physics*. Retrieved from <https://doi.org/10.1002/essoar.10503411>  
 1035 [.https://onlinelibrary.wiley.com/doi/10.1029/2020JA028345](https://onlinelibrary.wiley.com/doi/10.1029/2020JA028345) doi:  
 1036 10.1029/2020JA028345
- 1037 Manners, H., Masters, A., & Yates, J. N. (2018). Standing Alfvén Waves in Jupiter’s  
 1038 Magnetosphere as a Source of ~ 10- to 60-Min Quasiperiodic Pulsations.  
 1039 *Geophysical Research Letters*, *45*(17), 8746–8754. Retrieved from [http://](http://doi.wiley.com/10.1029/2018GL078891)  
 1040 [doi.wiley.com/10.1029/2018GL078891](http://doi.wiley.com/10.1029/2018GL078891) doi: 10.1029/2018GL078891
- 1041 Masters, A. (2018). A More Viscous-Like Solar Wind Interaction With All the Gi-  
 1042 ant Planets. *Geophysical Research Letters*, *45*(15), 7320–7329. doi: 10.1029/  
 1043 2018GL078416
- 1044 Masters, A., Achilleos, N., Bertucci, C., Dougherty, M. K., Kanani, S. J., Arridge,  
 1045 C. S., ... Coates, A. J. (2009). Surface waves on Saturn’s dawn flank mag-  
 1046 netopause driven by the Kelvin-Helmholtz instability. *Planetary and Space*  
 1047 *Science*, *57*(14-15), 1769–1778. Retrieved from [http://dx.doi.org/10.1016/  
 1048 j.pss.2009.02.010](http://dx.doi.org/10.1016/j.pss.2009.02.010) doi: 10.1016/j.pss.2009.02.010
- 1049 Masters, A., Eastwood, J. P., Swisdak, M., Thomsen, M. F., Russell, C. T., Ser-  
 1050 gis, N., ... Krimigis, S. M. (2012). The importance of plasma  $\beta$  conditions  
 1051 for magnetic reconnection at Saturn’s magnetopause. *Geophysical Research*  
 1052 *Letters*, *39*(8), 1–6. doi: 10.1029/2012GL051372
- 1053 Mauk, B. H., Haggerty, D. K., Jaskulek, S. E., Schlemm, C. E., Brown, L. E.,  
 1054 Cooper, S. A., ... Stokes, M. R. (2017). The Jupiter Energetic Particle  
 1055 Detector Instrument (JEDI) Investigation for the Juno Mission. *Space Science*  
 1056 *Reviews*, *213*(1-4), 289–346. doi: 10.1007/s11214-013-0025-3
- 1057 McComas, D. J., Alexander, N., Allegrini, F., Bagenal, F., Beebe, C., Clark, G., ...  
 1058 White, D. (2017). The Jovian Auroral Distributions Experiment (JADE)  
 1059 on the Juno Mission to Jupiter. *Space Science Reviews*, *213*(1-4), 547–643.  
 1060 Retrieved from <http://dx.doi.org/10.1007/s11214-013-9990-9> doi:  
 1061 10.1007/s11214-013-9990-9
- 1062 Moore, K. M., Yadav, R. K., Kulowski, L., Cao, H., Bloxham, J., Connerney,  
 1063 J. E., ... Levin, S. M. (2018). A complex dynamo inferred from the hemi-  
 1064 spheric dichotomy of Jupiter’s magnetic field. *Nature*, *561*(7721), 76–78.  
 1065 Retrieved from <http://dx.doi.org/10.1038/s41586-018-0468-5> doi:  
 1066 10.1038/s41586-018-0468-5
- 1067 Northrop, T. G., Goertz, C. K., & Thomsen, M. F. (1974). The magneto-  
 1068 sphere of Jupiter as observed with Pioneer 10: 2. Nonrigid rotation of the  
 1069 magnetodisc. *Journal of Geophysical Research*, *79*(25), 3579–3582. doi:

- 1070 10.1029/ja079i025p03579
- 1071 Nykyri, K., & Otto, A. (2001). Plasma transport at the magnetospheric boundary  
1072 due to reconnection in Kelvin-Helmholtz vortices. *Geophysical Research Let-*  
1073 *ters*, *28*(18), 3565–3568. Retrieved from [http://doi.wiley.com/10.1029/](http://doi.wiley.com/10.1029/2001GL013239)  
1074 [2001GL013239](http://doi.wiley.com/10.1029/2001GL013239) doi: 10.1029/2001GL013239
- 1075 Ozak, N., Cravens, T. E., & Schultz, D. R. (2013). Auroral ion precipitation at  
1076 Jupiter: Predictions for Juno. *Geophysical Research Letters*, *40*(16), 4144–  
1077 4148. doi: 10.1002/grl.50812
- 1078 Ozak, N., Schultz, D. R., Cravens, T. E., Kharchenko, V., & Hui, Y. W. (2010).  
1079 Auroral X-ray emission at Jupiter: Depth effects. *Journal of Geophysical*  
1080 *Research: Space Physics*, *115*(11), 1–13. doi: 10.1029/2010JA015635
- 1081 Quenouille, M. H. (1949). Problems in Plane Sampling. *The Annals of Mathematical*  
1082 *Statistics*, *20*(3), 355–375. Retrieved from [http://projecteuclid.org/](http://projecteuclid.org/euclid.aoms/1177706647)  
1083 [euclid.aoms/1177706647](http://projecteuclid.org/euclid.aoms/1177706647)[http://projecteuclid.org/euclid.aoms/](http://projecteuclid.org/euclid.aoms/1177729989)  
1084 [1177729989](http://projecteuclid.org/euclid.aoms/1177729989) doi: 10.1214/aoms/1177729989
- 1085 Quenouille, M. H. (1956). Notes on Bias in Estimation. *Biometrika*, *43*(3/4), 353.  
1086 doi: 10.2307/2332914
- 1087 Rae, I. J., Donovan, E. F., Mann, I. R., Fenrich, F. R., Watt, C. E., Milling, D. K.,  
1088 ... Balogh, A. (2005). Evolution and characteristics of global Pc5 ULF waves  
1089 during a high solar wind speed interval. *Journal of Geophysical Research:*  
1090 *Space Physics*, *110*(A12), 1–16. doi: 10.1029/2005JA011007
- 1091 Russell, C. T. (Ed.). (1992). *The Galileo Mission*. Dordrecht: Springer Netherlands.  
1092 Retrieved from <http://link.springer.com/10.1007/978-94-011-2512-3>  
1093 doi: 10.1007/978-94-011-2512-3
- 1094 Sandel, B. R., Smith, E. J., Davis, L., Jones, D. E., Coleman, P. J., Colburn,  
1095 D. S., ... Sonett, C. P. (1975). Jupiter’s Magnetic Field. Magnetosphere,  
1096 and Interaction with the Solar Wind: Pioneer 11. *Science*, *188*(4187), 451–  
1097 455. Retrieved from [https://www.sciencemag.org/lookup/doi/10.1126/](https://www.sciencemag.org/lookup/doi/10.1126/science.188.4187.451)  
1098 [science.188.4187.451](https://www.sciencemag.org/lookup/doi/10.1126/science.188.4187.451) doi: 10.1126/science.188.4187.451
- 1099 Vogt, M. F., Bunce, E. J., Kivelson, M. G., Khurana, K. K., Walker, R. J., Ra-  
1100 dioti, A., ... Grodent, D. (2015). Magnetosphere-ionosphere mapping  
1101 at Jupiter: Quantifying the effects of using different internal field models.  
1102 *Journal of Geophysical Research: Space Physics*, *120*(4), 2584–2599. doi:  
1103 10.1002/2014JA020729
- 1104 Vogt, M. F., Gyalay, S., Kronberg, E. A., Bunce, E. J., Kurth, W. S., Zieger, B.,  
1105 & Tao, C. (2019). Solar Wind Interaction With Jupiter’s Magnetosphere: A  
1106 Statistical Study of Galileo In Situ Data and Modeled Upstream Solar Wind  
1107 Conditions. *Journal of Geophysical Research: Space Physics*, 1–30. doi:  
1108 10.1029/2019JA026950
- 1109 Vogt, M. F., Kivelson, M. G., Khurana, K. K., Walker, R. J., Bonfond, B., Grodent,  
1110 D., & Radioti, A. (2011). Improved mapping of Jupiter’s auroral features  
1111 to magnetospheric sources. *Journal of Geophysical Research: Space Physics*,  
1112 *116*(3). doi: 10.1029/2010JA016148
- 1113 Weigt, D. M., Jackman, C. M., Dunn, W. R., Gladstone, G. R., Vogt, M. F.,  
1114 Wibisono, A. D., ... Kraft, R. P. (2020). Chandra Observations of  
1115 Jupiter’s X-ray Auroral Emission During Juno Apojove 2017. *Journal of*  
1116 *Geophysical Research: Planets*, *125*(4), e2019JE006262. Retrieved from  
1117 <https://onlinelibrary.wiley.com/doi/abs/10.1029/2019JE006262> doi:  
1118 10.1029/2019JE006262
- 1119 Weisskopf, M. C., Tananbaum, H. D., Van Speybroeck, L. P., & O’Dell, S. L. (2000).  
1120 Chandra X-ray Observatory (CXO): overview. *X-Ray Optics, Instruments, and*  
1121 *Missions III*, *4012*(July 2000), 2–16. doi: 10.1117/12.391545
- 1122 Wenzel, K. P., Marsden, R. G., Page, D. E., & Smith, E. J. (1992). The ULYSSES  
1123 Mission. *Astronomy and Astrophysics Supplement*, *92*(2), 207.
- 1124 Wibisono, A. D., Branduardi-Raymont, G., Dunn, W. R., Coates, A. J., Weigt,

- 1125 D. M., Jackman, C. M., ... Fleming, D. (2020). Temporal and Spectral Stud-  
1126 ies by XMM-Newton of Jupiter's X-ray Auroras During a Compression Event.  
1127 *Journal of Geophysical Research: Space Physics*, *125*(5), e2019JA027676.  
1128 Retrieved from <http://doi.wiley.com/10.1029/2019JA027676> doi:  
1129 10.1029/2019JA027676
- 1130 Wilson, R. J., & Dougherty, M. K. (2000). Evidence provided by galileo of ultra low  
1131 frequency waves within Jupiter's middle magnetosphere. *Geophysical Research*  
1132 *Letters*, *27*(6), 835–838. doi: 10.1029/1999GL010750
- 1133 Zhang, B., Delamere, P. A., Ma, X., Burkholder, B., Wiltberger, M., Lyon, J. G., ...  
1134 Sorathia, K. A. (2018). Asymmetric Kelvin-Helmholtz Instability at Jupiter's  
1135 Magnetopause Boundary: Implications for Corotation-Dominated Systems.  
1136 *Geophysical Research Letters*, *45*(1), 56–63. doi: 10.1002/2017GL076315